eral and ipsilateral projections. Considering the branching after the first branch point, the ipsilateral projections show longer (>1 mm; see scale bar in Fig. 7A) segments than the contralateral projections before further branching. These long segments are the stems of the forward and backward branches, for example, in Figures 5 and 6. As a result, the longest distances between first branch point and endpoint are found in ipsilateral rather than in contralateral projections. Comparison of the horizontal location of the endpoints within each dendrogram indicates the range of overall length differences within projections. It is of note that this range is a few millimeters for most projections (Fig. 7A–C,F), and that the largest ranges occur in ipsilateral projections (Fig. 7D,E).

## Distribution of endpoints in the parasagittal plane

Figure 8 shows the distributions of endpoints for contralateral (left column) and ipsilateral (right column) projections. Endpoints from one fiber are identified with the same colored symbol. The Figure 8 caption ranks the fibers by increasing CF. The two fibers for which both contralateral and ipsilateral projections were reconstructed are represented by the same symbols in left and right column: projections Contra 4 and Ipsi 2 (light blue inverted triangle, CF = 1498 Hz) and projections Contra 7 and Ipsi 5 (solid green triangle, CF = 2470 Hz). In all panels, the abscissa is the normalized rostrocaudal position of the endpoints, measured as illustrated in Figure 2 (virtually identical results are obtained if the distance along the z-axis, i.e., the distance between coronal sections, is used). The ordinate of the top two panels is the normalized dorsoventral position of the endpoints, measured as illustrated in Figure 1. These two panels therefore represent a standardized side view of the MSO. As expected, the endpoint positions are orderly arranged with low-CF fibers most dorsal and high-CF fibers most ventral (this is further analyzed in Fig. 9). The endpoints of a given fiber tend to be distributed in an elongated rostrocaudal strip. This is particularly the case in contralateral projections (Fig. 8A) and less so in ipsilateral (Fig. 8B) projections, which can be elongated (projection 1), restricted (projection 7), or patchy (projection 6). In contralateral fibers, seven of the nine fibers showed a broad rostrocaudal extent, spanning 40–60% of the nucleus, but importantly none of the fibers spans the entire nucleus.

The bottom panels show the key measurement: the axonal length accumulated between the first branch point for the projection from that side, and the endpoints. For contralateral projections (Fig. 8C), this length tends to increase for endpoints positioned more caudally in the nucleus. The solid lines are linear

contra 1 CF = 841 Hz

contra 3 CF = 1345 Hz

contra 5 CF = 2018 Hz
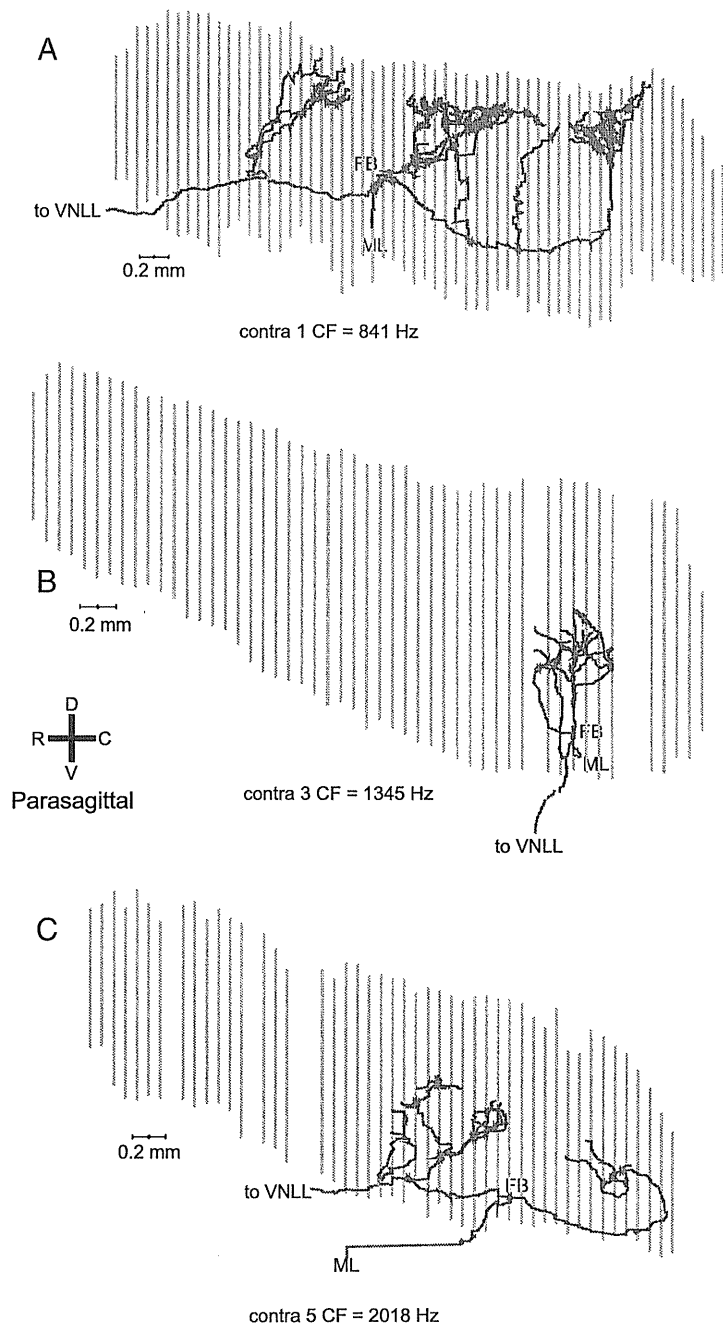
Figure 4. Parasagittal view of 3 more contralateral projections (A–C, with CFs indicated below each reconstruction) with a less clear-cut delay line configuration. In all cases, the FB is located near the center of the rostrocaudal range of EPs. The orientation shown in B applies to all panels. The color convention is as in Figure 3.

regressions; the dashed (black) line is the diagonal of equality. A "perfect" Jeffress delay line configuration would generate an endpoint distribution parallel to this line: the extra length incurred (ordinate) would equal the distance traveled rostrocaudally (abscissa). For six of nine contralateral fibers, the linear regression was significant ($p < 0.05$), with a correlation coefficient >0.80 in four of these six cases. The mean slope for the six cases was 0.91 (range, 0.54–1.65). The slope of the regression line was negative in one fiber (#3), for which the endpoints were distributed over a narrow rostrocaudal range. In two fibers (#1 and #9), the relationship was nonmonotonic, with a rostral patch of endpoints of
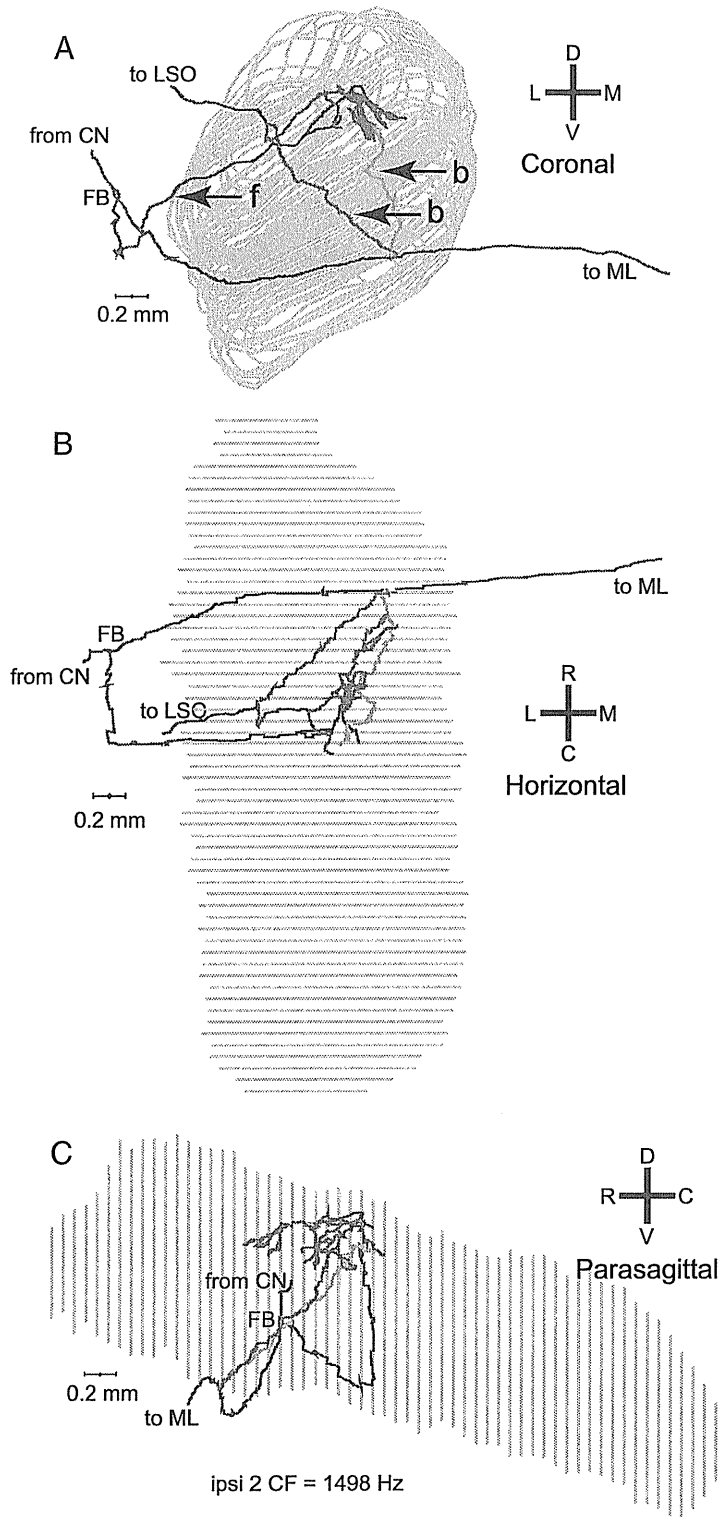
Figure 5. *A–C,* Coronal (*A*), horizontal (*B*), and parasagittal (*C*) views of a reconstructed projection of one fiber to the ipsilateral MSO. The coronal (*A*) and horizontal (*B*) views clearly show the two kinds of ipsilateral branches. One branch originates lateral to the MSO and projects forward (f, red) to it. Two branches originate after the axon has crossed the plane of the MSO and looped back (b, blue and green) to innervate the same region.

larger length than the endpoints just caudal to it. These are fibers whose axon crosses the midline at a rather caudal position as illustrated in Figure 3*C* (fiber #9, CF = 10,508 Hz) and Figure 4*A* (fiber #1, CF = 841 Hz).

The topography of the length distributions of ipsilateral projections (Fig. 8*D*) is strikingly inhomogeneous and different from the contralateral ones. The length gradient is mostly negative (i.e., in the opposite direction than the contrateral gradient) (Fig. 8, note the difference in ordinate scale between *C* and *D*). For comparison, the negatively sloped diagonal (large dashes) is shown, which shows the slope of a perfect Jeffress delay line configuration in the direction opposite to the one dominant in contralateral fibers. Linear regressions were significant for all seven fibers ($p < 0.01$). For two fibers (#6 and #7), the number of endpoints is small. Surprisingly, the slope is positive in three fibers.

Particularly for cases where the distribution of endpoints is restricted rostrocaudally (Fig. 8*D*, fiber #7, 8*C*, fibers #3 and #4), it is questionable that the presence of a slope in the linear regressions is of functional significance. Nevertheless, overall the length gradients are in accordance with the scheme proposed by Jeffress (1948), with a majority of contralateral projections showing a rostrocaudal increase in collateral length, and a majority of ipsilateral projections showing an inverse gradient.

Interestingly, fibers tend to project to either the rostral or caudal half of the MSO, particularly on the contralateral side (Fig. 8*A,B*, with the exception of the fibers indicated by the empty red triangles). Moreover, the length gradients most consistent with a Jeffress delay configuration are found in the rostral half, both in the contralateral and in the ipsilateral branches.

Note that only the slope of the regressions is relevant to the issue of delay lines, not the vertical offset on the ordinate. This offset reflects our (arbitrary) choice of the first branch point as the point of reference for the length measurement and is affected by the absolute length of the collateral branches. A branch that is longer than the rostrocaudal MSO dimension has endpoints with ordinate values >1, as is the case for several contralateral and many ipsilateral projections. However, addition of an identical length of axon to all collateral branches (see below, Estimates of rostrocaudal axonal delay, on calculation of differences in path length between ipsilateral and contralateral projections) moves all data points of a projection up along the ordinate without affecting the presence or absence of a rostrocaudal delay.

Tonotopic distribution along the dorsoventral axis
The rostrocaudal clustering of endpoints (Fig. 8*A,B*) allows us to project a map of input CFs onto the MSO. Figure 9 shows the

relationship between fiber CF and the normalized dorsoventral position of all endpoints. The endpoints contributed by one fiber are shown as a column of circles in Figure 9A, color coded for laterality. The asterisks show data points taken from the physiological data of Guinan et al. (1972, their Fig. 17). The solid circles and line show the position of the borders drawn in the summary tonotopic map of Guinan et al. (1972, their Fig. 21), at CFs of 1000, 4000, 10,000, and 20,000 Hz. There is a reasonable agreement between our data and those of Guinan et al. (1972). Much to our surprise, however, there is an upward convexity in the CF–position relationship. If low CFs were to take up a disproportionate amount of space of the MSO, relative to a logarithmic CF distribution, the relationship should be concave rather than convex: if one were to progress from dorsal MSO in a ventral direction and plot CF, there would initially be "slow" progression in CF, which would accelerate as one comes closer to the ventral pole. This is clearly not the case.

Because the cochlear map deviates from a logarithmic relationship at low CFs, we incorporate the CF–position relationship for the cochlea in the abscissa of Figure 8B, using Greenwood's equation (Liberman, 1982; Greenwood, 1990). The means and SDs of endpoint positions and the data points of Guinan et al. (1972) are replotted directly on a cochlear distance scale in Figure 9B. The data points again show an upward convexity. Predictions of the MSO CF–position relationship are now straight lines (green). The solid green line shows the relationship expected if all cochlear CFs were represented proportionally in the MSO: at low CFs, the data points tend to lie above this line. Another factor to take into account is that not all cochlear CFs appear to be represented in the MSO: the highest CF reported by Guinan et al. (1972) was 22 kHz. The dashed green line in Figure 8 shows the CF–position relationship expected if the cochlea were proportionally represented in the MSO except for its base, so that CFs >22 kHz are absent (~5 mm of the extreme base). Clearly, consideration of a limited CF representation does not alleviate the upward convexity. The prediction based on a limited CF range follows the slope of the map Guinan et al. (1972) reasonably well, but again the representation of the cochlear apex is compressed for our data, with the majority of low-CF data points lying above the dashed line.

The MSO tends to show curvature in the coronal plane (Figs. 1, 2, 6), and this curvature can be more pronounced at the dorsal
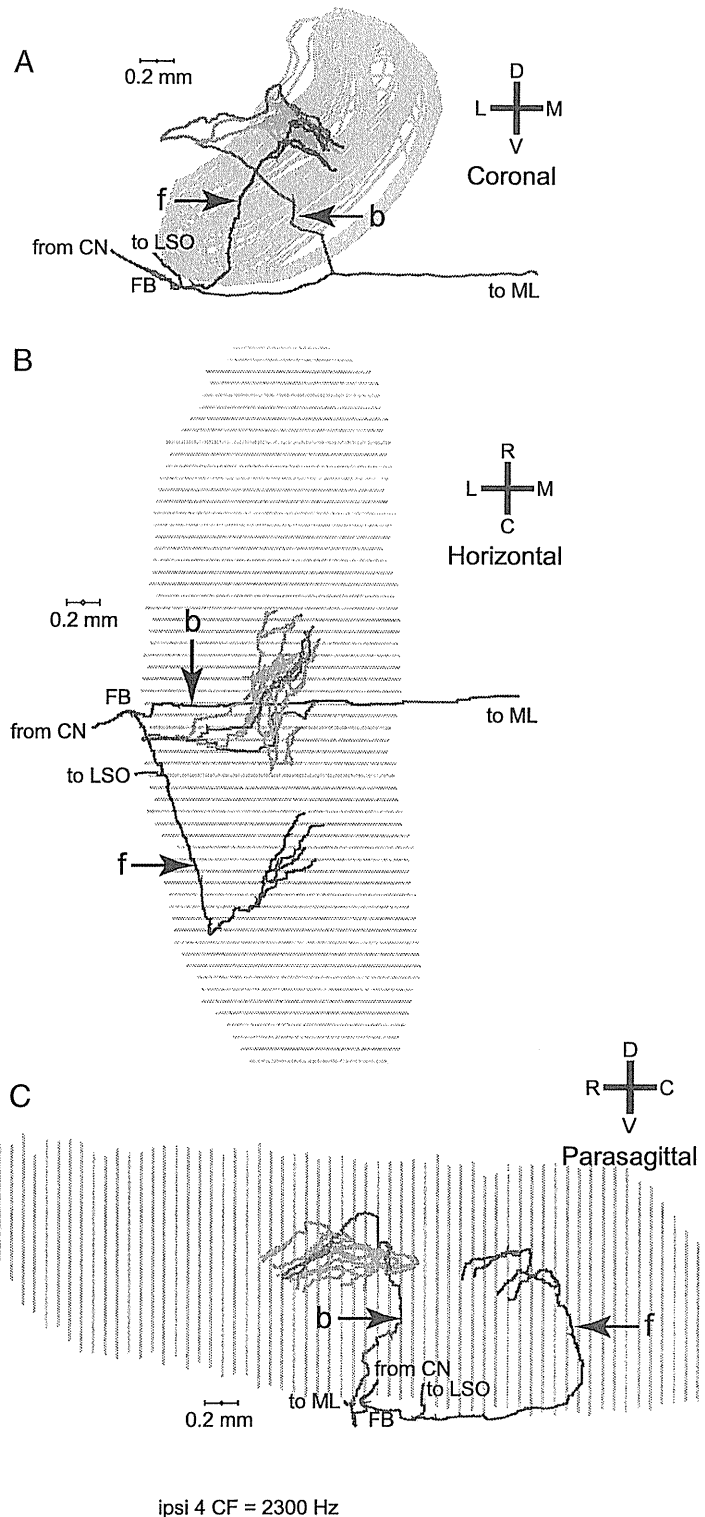
Figure 6. Another example of an ipsilateral MSO projections of one fiber. *A*, This fiber ran underneath the MSO (coronal view) and also formed forward (f) and backward (b) projecting branches. *B*, *C*, The horizontal (*B*) and parasagittal (*C*) views reveal that the branches innervate different rostrocaudal portions of the MSO. The backward branches (green and blue) innervated a more rostral portion of the MSO and covered more length of axon from FB than the forward branches.

pole (Fig. 1). Because our measure of dorsoventral location does not take curvature into account, we recalculated the dorsoventral positions in Figures 8, 9, and 10 taking the Euclidean distance of the endpoint to the ventral pole (as before), but now normalized

Contra   Ipsi
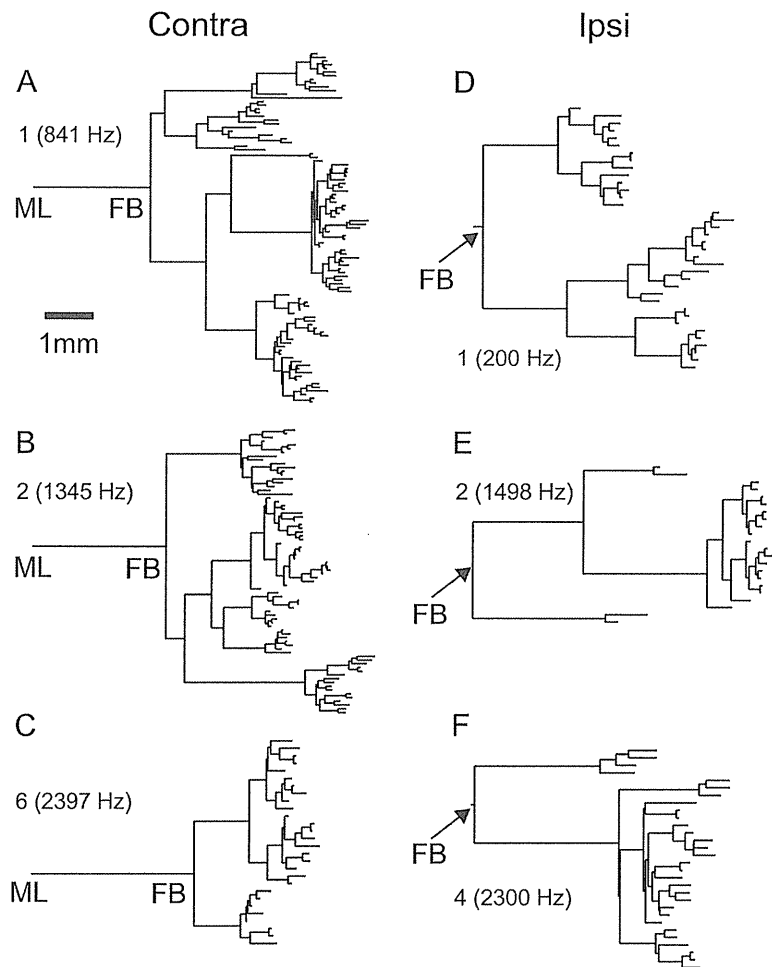
Figure 7. *A, B,* Dendrograms showing the branching pattern and length of axonal segments for three contralateral (*A*) and three ipsilateral projections (*B*). The scale bar in *A* applies to *A–F*. The horizontal dimension represents the axonal length of branch segments; the vertical dimension is only used to offset these segments and has no meaning with regard to length or order. Fiber number and CF are indicated for each projection. Cross-linking to previous figures with computerized reconstructions is as follows: *A* = Figure 4*A*; *B* = Figures 1 and 2; *C* = Figure 3*A*; *D* = Figure 5 of Smith et al. (1993); *E* = Figure 5; *F* = Figure 6.

fibers showing forward branches (Fig. 10 legend, + symbols), these branches give endpoints located more lateral than the backward branches (projections 2, 4, and 6).

Axon diameter and conduction velocity
The analysis so far has concerned branching patterns, endpoint position, and axon length. Other factors than axonal length contribute to the time delay in action potential propagation; most importantly myelination, axon diameter, and internodal distance. The only additional factor we can assess in our material is axon diameter, be it only crudely for the various reasons pointed out in Smith et al. (1993). Diameters were measured at each axonal (x,y,z) position entered. Using these measurements, we calculated the mean diameter of each "segment," which is the part of an axon between neighboring branch points; branch points and endpoints; or midline and branch point. Figure 11 shows the mean diameter as a function of distance from the midline (Fig. 11*A*) for contralateral projections, and from the first branch point (Fig. 11*B*) for ipsilateral projections. These graphs are obtained by moving from left to right across the dendrograms (Fig. 7), and tallying and averaging all the segment diameters that are present for a given length from the starting point (Figs. 2–4, ML, 5, 6, FB). Close to the starting points, the mean diameter jumps in large steps because few branches are present, but the trace becomes smoother as more branching occurs. There is a general decrease in axon diameter toward the endpoints.

To compare diameters of contralateral and ipsilateral branches, we first determined the number of segments of a given diameter (bin size, 0.1 μm). Dividing by the number of contributing fibers (9 for contralateral and 7 for ipsilateral projections), we obtain the average numbers shown in Figure 12, *A* and *B*. The diameters are largely between 1 and 3 μm; the mean is 1.8 μm for both distributions (*t* test, $p = 0.27$). For the contralateral projections, the axonal segments include all segments of projections into the contralateral MSO arising after the midline crossing, while for the ipsilateral projections they include all segments projecting into the ipsilateral MSO after the first branch point. The reason that we included the "extra" segment between midline and first branch point in the contralateral projections is that the midline gives an "absolute" reference that can be identified in each animal, which allows an estimate of path length for the axon in the contralateral hemibrain. These proximal segments are shown in black in Figure 12, *A* and *C*. Removal of these segments did not affect the lack of a statistically significant difference between the diameter distributions of contralateral and ipsilateral projections ($p = 0.13$).

Numerically, the final segments, shown in gray in Figure 12, dominate the histograms, due to the profuse branching once the collaterals reach the tonotopic layers where they form their endpoints. Because the axons progressively taper (Fig. 11) and much

to the sum of the distance of the endpoint to the ventral and dorsal poles (i.e., the normalization was now to the sum of the line segments EP–VP and EP–DP). This recalculation caused only minor shifts in ordinate position and did not remove the bias of low-CF data points above the green lines in Figure 9*A,B*.

Distribution of endpoints in the mediolateral dimension
Figure 10 shows the normalized mediolateral versus dorsoventral distribution of endpoints. As commented on in Materials, determination of the mediolateral endpoint position is inherently inaccurate. Relative to its small width, the medial and lateral border of the MSO cannot be determined with much precision (note that, on the square axes of Fig. 10, the mediolateral dimension is much magnified relative to the dorsoventral dimension, approximately by a factor 3.6). The uncertainty becomes particularly large for endpoints located close to the dorsal or ventral pole. This is visible in Figure 10: the mediolateral spread of points increases toward the dorsal pole. Nevertheless, as expected (Stotler, 1953), the contralateral endpoints occupy dominantly a medial position, and the ipsilateral endpoints a lateral position. Of interest is that the forward and backward branches of the ipsilateral projection seem to occupy the same dorsoventral (tonotopic) but not mediolateral position. For the four

of the delay must accrue at the distal branches, it is of interest to compare contralateral and ipsilateral distributions for the final segments. Again, there is no difference in the distributions for contralateral and ipsilateral fibers ($p = 0.26$).

Next, to visualize the relationship between diameter and length of segments, we summed the lengths for all segments with a given diameter for all fibers (bin size 0.1 μm) and normalized to the number of contributing fibers (9 for contralateral and 7 for ipsilateral projections). Thus, Figure 12, C and D, shows average segment length of a given diameter for contralateral and ipsilateral projections, respectively. Statistical comparison shows that at none of the bins for which both contralateral and ipsilateral values are present is there a significant difference in segment length (t test, $p > 0.05$).

From the axon diameter and length, estimates for conduction speed and time can be calculated. We followed the method of Beckius et al. (1999) to estimate conduction time as follows:

$$L/(d^*RV), \qquad (1)$$

with L being the length (in millimeters) of axon between two branch points, d being the average diameter (in micrometers) of that segment, and RV being an experimentally derived constant (9.167 mm/ms/ μm) (Waxman and Bennett, 1972). For each endpoint, the conduction times of all segments interposed between that endpoint and a fixed starting point were added.

In Figure 13 we show the estimated conduction times for all endpoints using as starting points the midline (Fig. 13C, contralateral projections) or the first branch point (Fig. 13D, ipsilateral projections) against the length of axon traversed to reach these endpoints. The relationship is very orderly; in all fibers, linear regression (data not shown) of length on conduction time was significant ($p < 0.001; p < 0.01$ in one fiber). This result is not surprising and may seem trivial because of the proportionality of estimated conduction time to length in Equation 1. However, if the average diameter to reach one endpoint were larger than that to reach another endpoint of the same tree, the conduction time would be shorter even if the average length were the same (Fig. 13A). Likewise, there could be a length difference that is compensated by a difference in axon diameter (Fig. 13B). The linear distributions of endpoints in Figure 13, C and D, show that d (Eq. 1) is "well behaved" in the sense that diameter decreases similarly with distance in all branches and that there is no systematic effect of diameter that offsets or enhances the "delay line effect" of the branching pattern. The slope of the linear regressions (data not shown) was on average 19.3 m/s for the contralateral and 17.9 m/s for the ipsilateral projections (ranges: 14–26 m/s for Contra; 13–21 m/s for Ipsi).
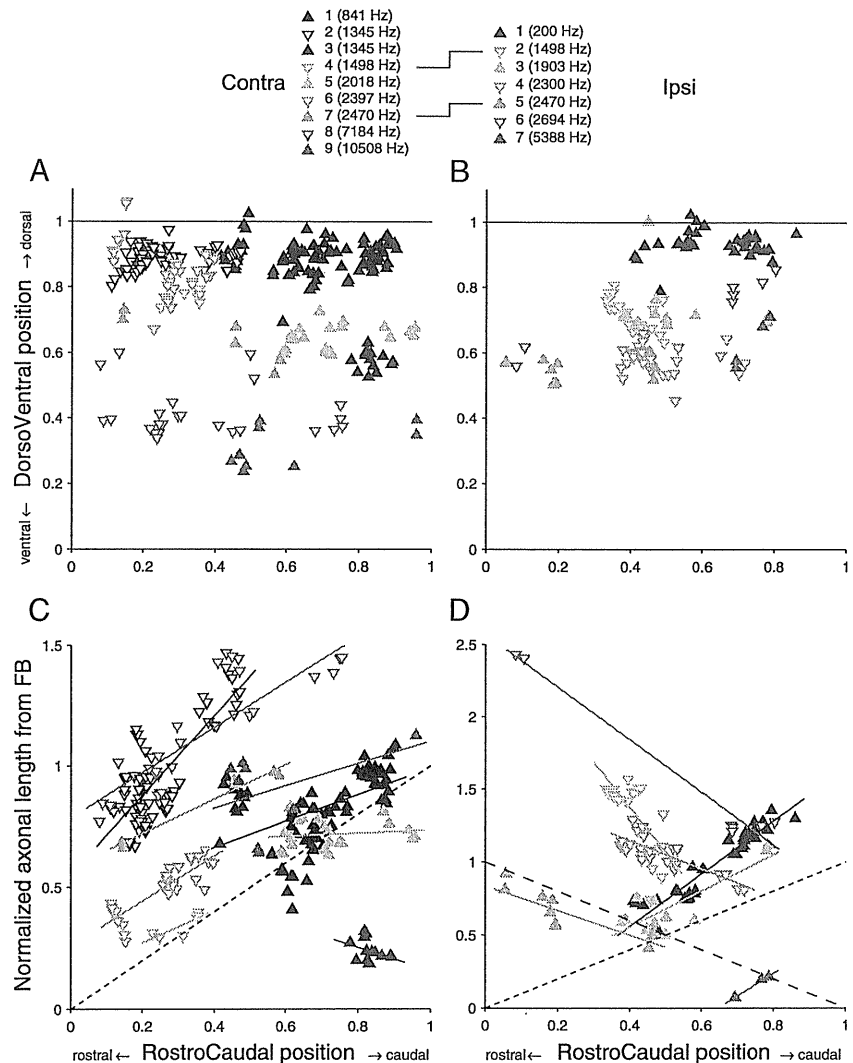

Figure 8. Length gradients along the rostrocaudal axis of the MSO. *A, B,* Distribution of endpoints of contralateral (*A*) and ipsilateral (*B*) projections on normalized MSO axes. *C, D,* Axonal length from FB to the different endpoints. Solid lines are linear regressions. The diagonals with short dashed lines indicate the diagonal of equality; the diagonal with the long dashed lines indicates the slope expected for an opposite length gradient. The caption shows the symbols and color used for the endpoints originating from the different fibers, numbered for increasing CF and reused in subsequent figures. The lines between left and right symbol captions indicate the two fibers for which both the contralateral and ipsilateral projections were reconstructed.

Note that these slopes do not give conduction speeds, but rather the speed at which excitation would "sweep" through the endpoints. If all endpoints were arranged in an orderly fashion as in Jeffress' model so that the endpoints with the shortest axonal length were located (e.g., most rostrally and those with the longest length most caudally), the range of conduction times spanned by the endpoints of one axon would equal the range of its x-values in Figure 13, C and D [e.g., 220–350 μs for the contralateral projection (#1), represented by the black triangles in C; i.e., a range of 130 μs]. However, as already shown in Figure 8, C and D, the arrangement of endpoints is not that orderly. Again taking projection #1 as an example, it can be seen in Figure 8C that endpoints with similar axonal length occur over a significant rostrocaudal range. We return to this point in the section below, Estimates of rostrocaudal axonal delay (Fig. 14).

The lines in Figure 13, C and D, connect starting points, branch points, and endpoints of each projection. The slope of each line equals the speed of the corresponding segment. This
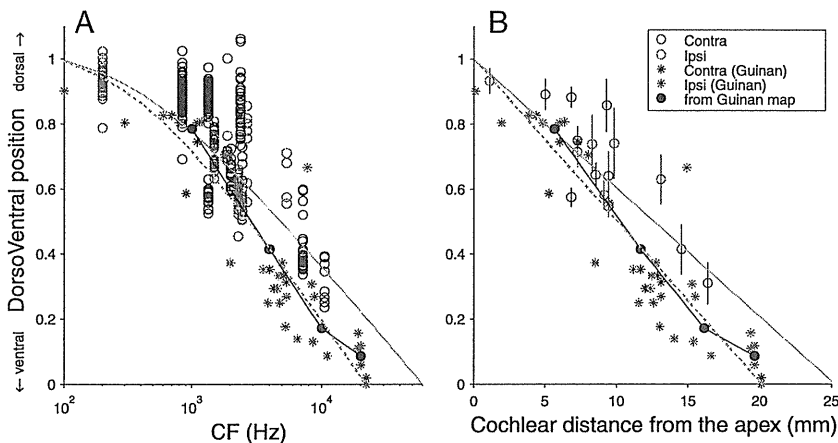
Figure 9. Tonotopic compression of low frequencies in MSO. *A*, *B*, The dorsoventral location, normalized to the dorsoventral extent of the MSO, is shown for all endpoints of all reconstructed fibers on a logarithmic CF abscissa (*A*) and for their mean and SD on a cochlear distance abscissa (*B*). Each circle in *A* indicates a single endpoint (blue, contralateral fiber; red, ipsilateral fiber). The asterisks and the black circles and line show extracellular and summary data from Guinan et al. (1972) (see main text). The green lines are predicted relationships based on the cochlear tonotopic map, based on Greenwood's formula (Greenwood, 1990). The solid green line is the prediction for a full representation of all CFs; the dashed line is for a representation limited to ≤22 kHz. The endpoints at low CFs cluster above the green lines. If low CFs were over-represented in MSO, those endpoints would be expected to cluster below rather than above the green lines.
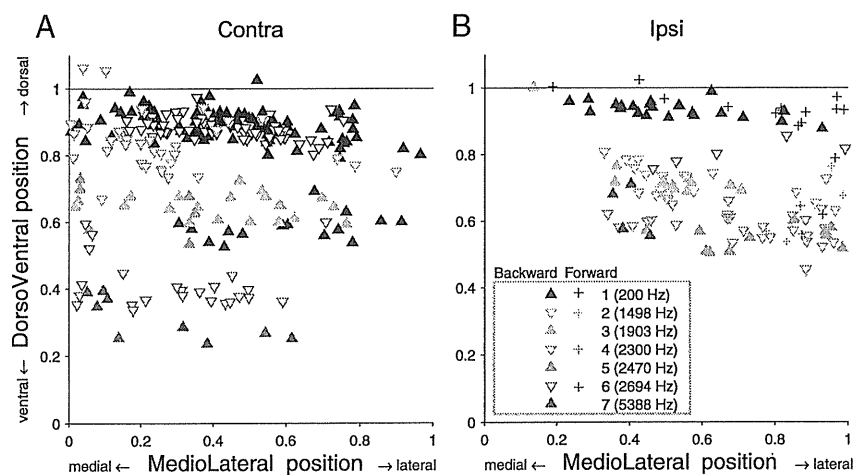
Figure 10. *A*, *B*, Distribution of endpoints in the coronal plane, for contralateral (*A*) and ipsilateral (*B*) projections. Symbol use for *A* is as in Figure 8. The "Backward" and "Forward" in *B* refer to backward and forward branches, as illustrated in Figures 5 and 6.

slope decreases with increasing distance from the starting point, due to the gradual decrease in axon diameter, and gives rise to the general curvature in the data. For each endpoint, the length traversed divided by the estimated conduction time gives an estimate of the average speed from starting point to each endpoint (this speed equals the slope of a line connecting the endpoint to the origin in Fig. 13*C,D*, illustrated for the diagrams in Fig. 13*A,B* with dashed lines). The ranges of estimated speeds are shown in Fig. 13*E–G*. They are similar across endpoints and CFs, and are also very similar for contralateral and ipsilateral fibers (means, 20.1 and 19.3 m/s, respectively), when taking midline (Fig. 13*E*) and first branch point (Fig. 13*G*), respectively, as a starting point. When the contralateral side is also referenced to the first branch point rather than to the midline (Fig. 13*F*), the estimated conduction speed drops to 18.4 ms/s on average. This reflects the long distance (several millimeters) of the segment from midline to first branch point in contralateral fibers (Figs. 7*A–C*, 11*A*) and

the large diameter of that segment (Fig. 11*A*), while the ipsilateral projection tends to sustain long (Fig. 7*E,F*) and large-diameter (Fig. 11*B*) forward and backward segments after the first branch point. In summary, the overall distribution of axon diameter and its progression along the axon is similar in contralateral and ipsilateral projections.

### Estimates of rostrocaudal axonal delay

The main quantitative check so far regarding Jeffress' (1948) hypothesized axonal delay lines was in Figure 8, *C* and *D*, which examined length as a function of rostrocaudal position. In a similar format, Figure 14, *A* and *B*, replots the data directly in dimensions of time and space: estimated conduction time, calculated from both diameter and length, versus rostrocaudal position in micrometers from the most rostral MSO section. The abscissa origin coincides with the section containing the rostral pole, while the location of the section of the caudal pole is indicated by an asterisk at the caudal end of a linear regression line drawn through all the endpoints of each projection. As expected from the general trend of a graded decrease in axon diameter (Figs. 11–13), the relationships of Figure 8, *C* and *D*, are preserved in Figure 14, *A* and *B*. Thus, it does not appear to be the case that afferent branch diameter is regulated to fine tune delay lines based on length, at least not at the level of assessment of diameter that is possible with our material.

To summarize the regression data on estimated conduction times (Fig. 14*A,B*) and measured length gradients (Fig. 8*C,D*), Figure 14*C* shows the slopes of the linear regressions in these figures. Abscissa values of 1 and −1 indicate "perfect" slopes of delay, where the extra length of axon is identical to the extra distance in rostrocaudal (or caudorostral) direction (Fig. 8, compare diagonals in *C* and *D*). All significant (large symbols) contralateral projections, as well as three ipsilateral projections, contribute data to the upper right quadrant. The data points in the lower left quadrant consist only of ipsilateral projections, which form a length gradient in the caudorostral direction. Note that the most extreme positive and negative values are found in the ipsilateral projections. Also of note are the rather modest values of the estimated delays. To map the physiological range of delays (300–400 μs in the cat) (Roth et al., 1980) on the length of MSO (3–4 mm) (Fig. 14*A,B*), the interaural delay accrued per millimeter should be ~100 μs. The ordinate values in Figure 14*C* show that the estimated "monaural" delays fall short for the contralateral projections. The ipsilateral delays come close but are in the wrong direction for the positive values, and for the negative values some of the projections are limited in spatial extent (Fig. 14*B*). In Jeffress' (1948) scheme, it is the combination of ipsilateral and con-

tralateral axonal delays that establish the map of interaural delays. Thus, even if insufficient by themselves, a combination of the contralateral delays (triangles in upper right quadrant) and some of the ipsilateral delays (squares in the lower left quadrant) could sum to the needed physiological range of delays. The estimated delays are replotted versus CF in Figure 14D. For each fiber, the (extrapolated) delay at the rostral pole of the MSO is anchored to the horizontal line at 0 delay, and a vertical line is drawn to the extrapolated delay at the caudal pole. The line extends to positive delays for nearly all contralateral projections (triangles), and also for the four ipsilateral projections (squares) with negative slopes in Fig. 14B; these projections could all contribute to the pattern of interaural delays reported by Yin and Chan (1990). The individual data points show the estimated delays for individual end-points, and the short horizontal bars delimit the range of delays of the linear regression over which endpoints are actually found. The gray rectangle approximates the range of physiological delays (400 μs) that is presumed to be represented in the MSO of one side. Again, the range of delays subserved by contralateral projections is small, but could suffice when combined with the ipsilateral delays.

As was first reported in the guinea pig (McAlpine et al., 2001), the distribution of best delays in the inferior colliculus of the cat (Hancock and Delgutte, 2004; Joris et al., 2006) does not follow the shaded gray rectangle, but is largely restricted to the area defined by horizontal line at zero delay and the upper hyperbole at half a characteristic period (CF^{-1}), and this is also the case for recordings of the MSO in rodents (Brand et al., 2002; Pecka et al., 2008). Binaural recordings have shown that best delays have a specific distribution pattern that is constrained by the upper hyperbole and the horizontal. Taken at face value, the axonal delay estimates of the present results are not consistent with the pattern of binaural delays thought to be represented in the MSO. There is no suggestion in the distribution of estimated delays toward larger delays at low than at high CFs.

Figure 14 focuses on the ranges of estimated delay, taking as anchor points the midline (Fig. 14A), the first branch point (Fig. 14B), or the rostral pole (Fig. 14D). The inherent longer path length of contralateral projections combined with the similarity of axon diameter in contralateral and ipsilateral projections (Fig. 12) implies a systematic additional delay for the contralateral inputs. Comparison of the entire contralateral and ipsilateral delay generated by an axon is difficult because that would require backfilling of the soma and labeling of the entire projection to both contralateral and ipsilateral MSO. However, we can make an estimate of the difference in delay between contralateral and ipsilateral inputs. Taking into account that individual fibers project both contralaterally and ipsilaterally, and, assuming mirror symmetry between left and right sides of the brainstem, we only need to increase the contralateral delay estimates of Figure 14A (made with respect to the midline) with the delay estimated for the axonal segment between the ipsilateral first branch point and the midline [Fig. 15B, distance from ipsilateral first branchpoint (FBi) to midline]. We could trace this segment in all ipsilaterally projecting fibers. The average segment length was 4994 μm
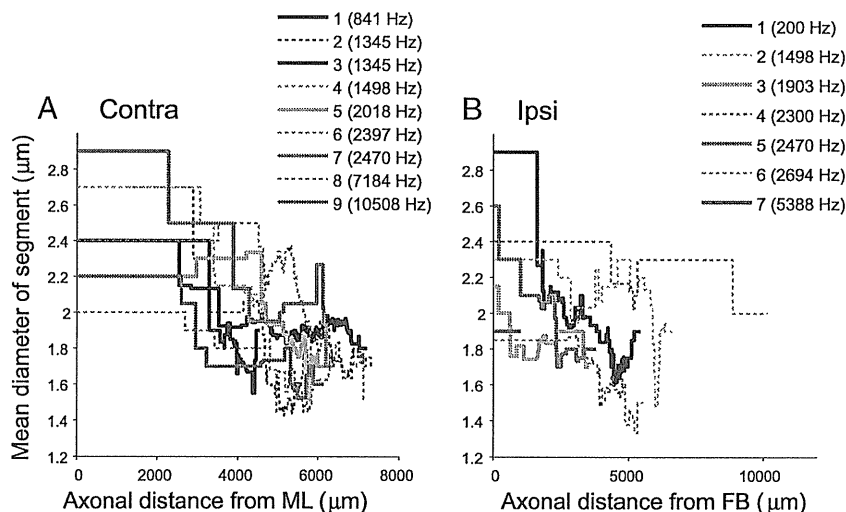

Figure 11. A, B, Average axon diameters decrease as a function of distance from the midline (A, Contra projections) or from the first branch point (B, Ipsi projections).
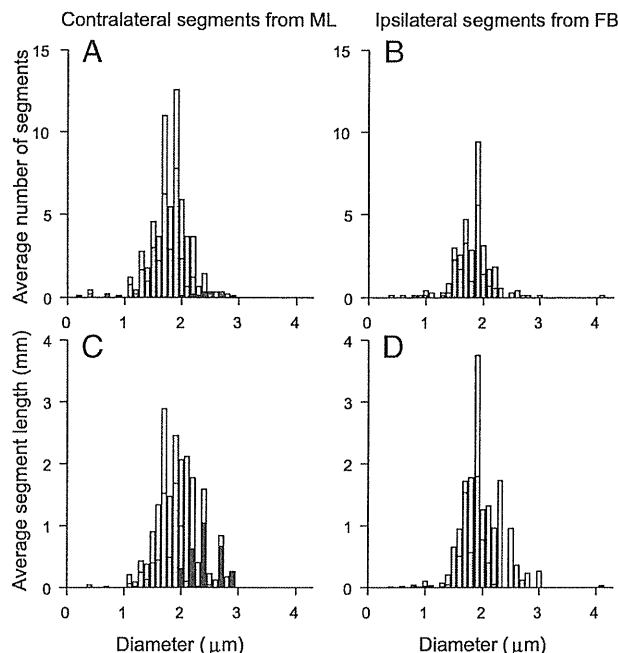
Figure 12. $A–D$, Distribution of axon diameters does not differ between contralateral (A, C) and ipsilateral (B, D) projections. The top histograms show the average number of segments with a given diameter (0.1 μm bins); the bottom histograms show the corresponding average length (in mm) at that diameter. All histograms are averages calculated for the entire population of contralateral and ipsilateral fibers, normalized to the total number of fibers included. The starting segments were ML (contralateral fibers) and FB (ipsilateral fibers). White bars include all the segments from starting segment to endpoints. Gray bars show length of most distal segments, terminated by endpoints. Black bars show length of most proximal segments, which contain ML (contralateral fibers only).

(range, 3748–6106 μm), and the average diameter was 2.6 μm (range, 1.9–3.0 μm), yielding an average extra delay (Eq. 1) of 221 μs (range, 139–351 μm). Thus, on average the endpoint delay estimates in Figure 14A would need to be increased by 221 μs. The value of 221 μs may be an overestimate because the axon diameters of our small sample seem to be an underestimate (Eq. 1); larger axon diameters at the midline were reported by Smith et al. (1993) (2.5–5 μm) and Brownell (1975) (3–5 μm).
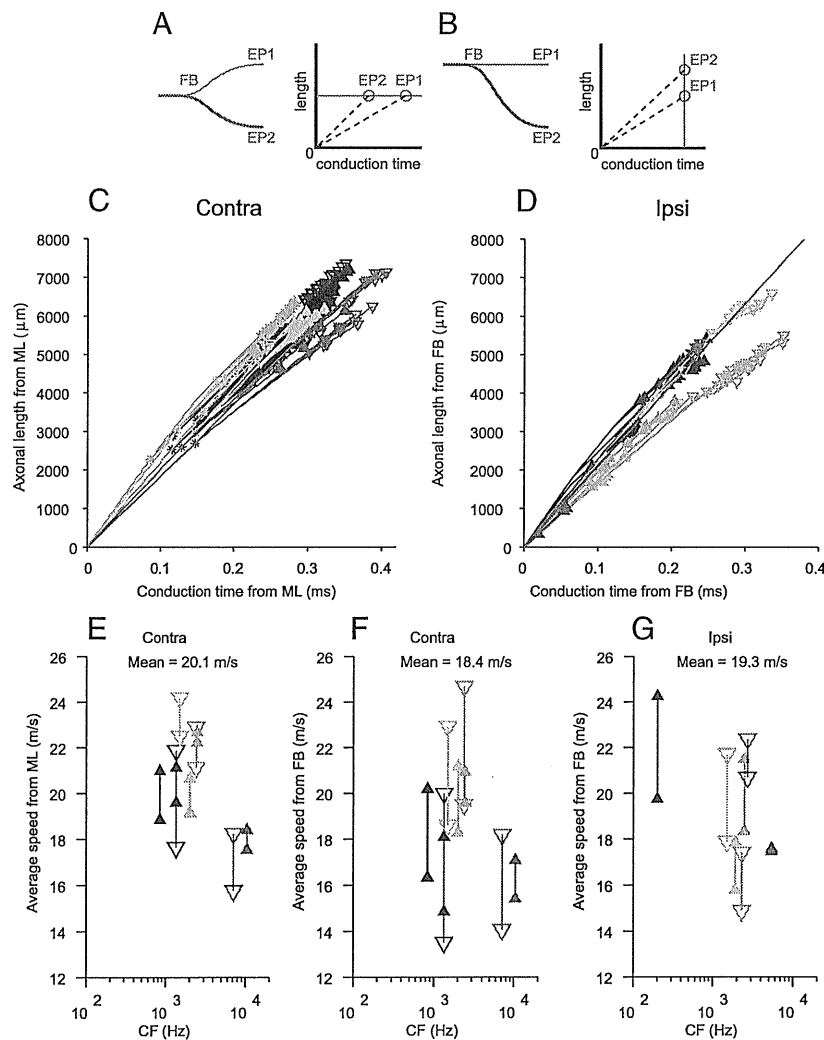
Figure 13. Axonal length is linearly related to estimated conduction time. Axonal lengths are measured as in Figures 7 and 11. Conduction time for each endpoint is the sum of conduction times of all segments leading up to that endpoint, calculated from segment length and diameter (see text). Diagrams in *A* and *B* illustrate configurations that would result in nonsloping relationships. *C,* Length and time for contralateral projections, using ML as reference point. *D,* Length and time for ipsilateral projections, using FB as reference point. One outlying endpoint is clipped off. *E, F,* Estimated average conduction speeds for all endpoints. This is the slope of the lines connecting the endpoints in *C* and *D* with the origin at (0,0), as illustrated with the dashed lines in *A* and *B*. *E–G,* Reference point at (0,0) was ML (*E*) or FB (*F, G*). Color code and symbols are identical to Figures 8 and 10. The symbols indicate the lowest and highest speed for the endpoints of a given fiber.

The values of Beckius et al. (1999) (slightly >2 μm) are comparable to our own.

Note that inclusion of this extra delay does not alleviate the problem pointed out in Figure 14*D*, since it adds a constant delay common to all endpoints of a given fiber and does not increase the range of available delays provided by a given fiber. Figure 15*A* shows the estimated average (symbols) and range (lines) of path lengths from the last common axonal point (FBi) to all endpoints, as a function of CF, using the average of 4994 μm for the distance from FBi to midline calculated above. On average, the contralateral pathway from FBi onward is 10.78 mm, and the ipsilateral pathway is 4.21 mm. Incorporating the measured diameters, the average delay from the first ipsilateral branch point to MSO is an estimated 511 μs for the contralateral projections and 220 μs for the ipsilateral projections. Thus, the difference in path length is on average 6.57 mm, which generates an extra delay for the contralateral projection of an estimated 290 μs. Notwith-

standing the uncertainty of its exact value, this extra delay must contribute to the contralateral bias of best delays seen in all studies of the MSO and inferior colliculus. It is interesting to observe that this value is similar to the ~200 μs extra contralateral delay in the lateral superior olive, estimated with different physiological methods (Joris, 1996; Joris and Yin, 1998; Tollin and Yin, 2005).

Axonal delay in the dorsoventral dimension

Differences in the CF of contralateral and ipsilateral inputs converging on MSO neurons have been proposed as a source of internal delays (Schroeder, 1977; Shamma, 1989; Bonham and Lewis, 1999). Cross-correlation analysis of responses of auditory nerve fibers revealed that disparities of a fixed distance on the cochlear basilar membrane generate a wider range of internal delays at low than at high CFs, in accord with the pattern of internal delays inferred from recordings in the inferior colliculus (Joris et al., 2006). However, to explain not only the decrease in the range of best delays with CF, but also the decrease in mean best delay with CF, an additional mechanism is needed. Because most contralateral projections approach the MSO from a rostral and ventral position (Figs. 2*C*, 3*A*,*B*), it was hypothesized (Joris et al., 2006) that the longer distance toward the dorsal (low-CF) pole of the MSO compared with the ventral (high-CF) pole perhaps causes a systematically longer delay for low-CF than for high-CF contralateral inputs. This hypothesis is illustrated with the schematic in Figure 15*C*. In Figure 15*D*, we show the mean and SD of the axonal lengths from midline to endpoint for all contralateral projections as a function of fiber CF (for individual data points, see Fig. 13*C*). There is no hint of a CF dependency showing longer lengths for the most dorsally projecting fibers (lowest CFs). The low-CF (Fig. 15*E*) and high-CF (Fig. 15*F*) projections illustrated in coronal view show that the tilting of the dorsal edge of the MSO toward the midline, combined with the angling of the contralateral low-CF fibers, is such that indeed no differential delay would be expected relative to the more ventral, high-CF projections. There is therefore no evidence in our data for a length gradient along the dorsoventral dimension in the excitatory inputs from the contralateral ear.

Discussion

Sensitivity to temporal differences in the sounds to the two ears provide a powerful model system to study neural temporal processing. Putative axonal delay lines have been an important component of models and of theorizing regarding such processing (Jeffress, 1948; Licklider, 1959; McFadden, 1973; Carr and Konishi, 1988; Cariani, 2004). There is general agreement that sensi-

tivity to ITDs involves internal delays causing a temporal shift of inputs from one ear relative to the other. What is increasingly questioned is the proposal (Jeffress, 1948) of a conversion of a temporal code to a place code by virtue of axonal delay lines. We quantitatively reanalyzed projection patterns of spherical bushy cells of the AVCN to MSO (Smith et al., 1993). The main findings of that study hold up and are consistent with a later study (Beckius et al., 1999); axonal configurations that are qualitatively of the nature surmised by Jeffress (1948) are found for contralateral projections, and less clearly for ipsilateral projections. Nonetheless, these configurations are not consistent in a simple form with the binaural data that have become available since.

Previous studies

The two previous reports on anatomical delay lines in the cat have complementary virtues. The power of the data of Smith et al. (1993) is that their 18 axons were physiologically characterized and that the labeling was unambiguously from single fibers, but filling was incomplete so that, typically, projections on only one side could be reconstructed. Their report showed one contralateral and one ipsilateral computer reconstruction. Beckius et al. (1999) labeled a large number of axons by injecting the rostral pole of the AVCN, of which 17 well filled axons (from 2 animals) were quantitatively reconstructed, with 7 reported in detail. Disadvantages of that material are the absence of physiology and the difficulty in connecting pieces across sections. Both studies have few data at very low CFs, where the largest best delays are observed. Best frequencies at the site of injection in Beckius et al. (1999) were estimated at ~1.5–1.75 kHz, but the tonotopic layering of the projections suggests that the actual range of CFs was much larger. In Smith et al. (1993), only two fibers had CF <1 kHz.

Despite differences in technique, the two studies were consistent, finding caudally directed delay line patterns contralaterally and a complex, less systematic pattern ipsilaterally. Quantitative analysis allowed Beckius et al. (1999) to discern a weaker length gradient in ipsilateral branches, in a direction opposite to the contralateral pattern. The quantitative analysis presented here is largely consistent with that of Beckius et al. (1999). The main additional findings concern the ipsilateral projections. We found caudally directed delay lines in three (of seven)
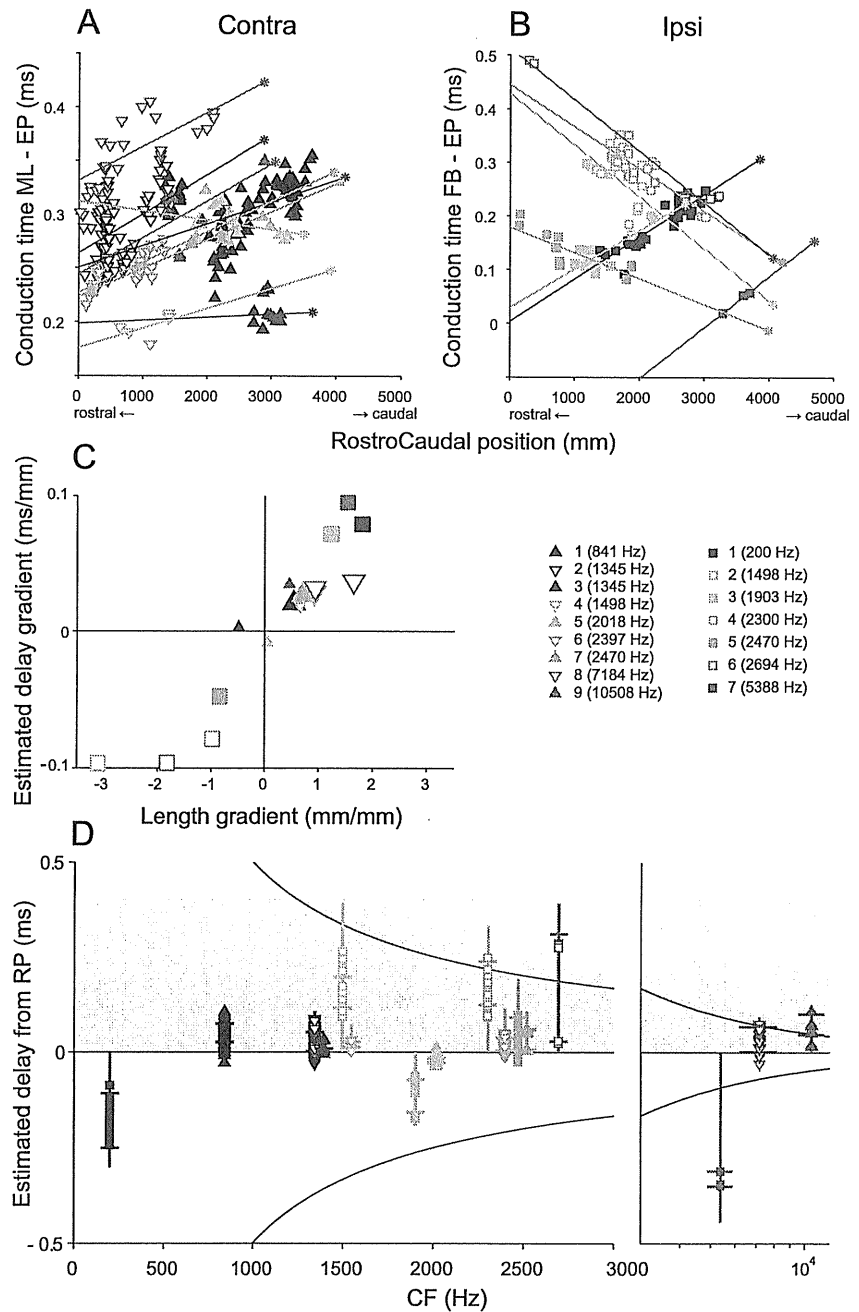
Figure 14. Rostrocaudal gradients of conduction time. *A, B,* Relationship between estimated conduction time and location of EP in rostrocaudal dimension in contralateral (*A*) and ipsilateral (*B*) fibers. The abscissa is zeroed to the position of the most rostral section in which MSO could be identified, and abscissa values are the distance of endpoints to that most rostral section. Ordinate values are the estimated conduction times from the midline (*A*, contralateral projections) or first branch point (*B*, ipsilateral projections). Solid lines are linear regressions. The asterisks at the end of each line indicate the most caudal MSO section. Note that the ordinate in *B* has a wider range than in *A*. *C,* Summary of regression slopes of Figure 8, *A* and *B* (abscissa), and of *A* and *B* (ordinate). Large symbols indicate values that are significant for both abscissa and ordinate. Contra 4 showed significance (*p* < 0.05) for length but not for delay; and vice versa for Contra 9. *D,* Relationship between estimated delay and CF. The anchor point of each colored vertical line at 0 delay represents the RP of the MSO. The opposite end shows the extrapolated delay at the CP (corresponding to the delay accumulated between RP and the asterisk in *A* and *B*). The small horizontal bars show the range of delays of the linear regression over which endpoints are present. Symbols and lines at positive delays, in the shaded region, are for fibers with a pattern consistent with the trend observed by Yin and Chan (1990); these are the fibers with positive slope in *A* or negative slope in *B*. Symbols and lines at negative delays are for fibers with an opposite branching pattern (negative slope in *A* or positive slope in *B*). Hyperbolic curves indicate the π limit (i.e., the extent of one period equaling CF^{-1}). The scale of the abscissa is linear in the left panel and logarithmic in the right panel.
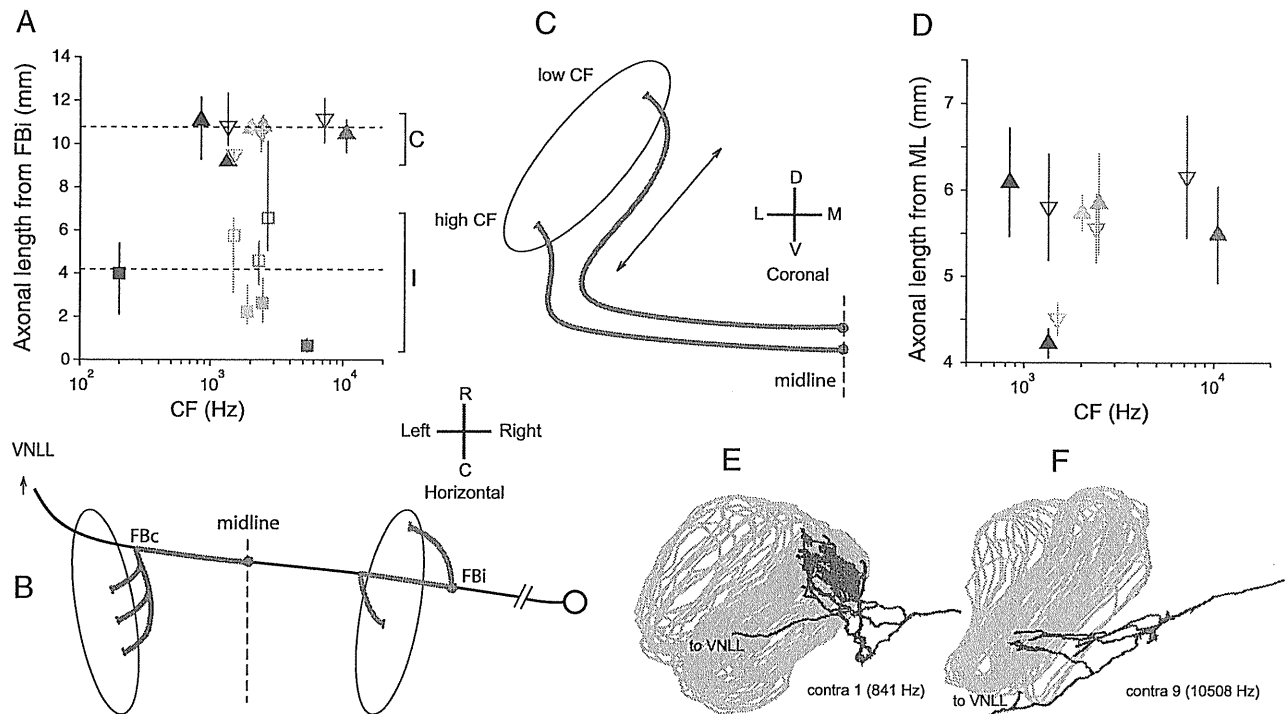
Figure 15.   A, B, Differences in path length between ipsilateral and contralateral inputs. A, Estimated average and range of lengths for contralateral and ipsilateral projections between the FB of the ipsilateral MSO projection and the endpoints. Dashed lines show overall contralateral (C) and ipsilateral (I) mean. B, Schematic of the measurement. The length of the trajectory between midline and contralateral endpoints (red), or between FBi and endpoints (green), was measured (same values as in Fig. 13C,D). To estimate the difference in length of contralateral and ipsilateral inputs, the red segment needs to be augmented by the distance FBi to midline: we use the average measured on ipsilateral projections (4994 µm, see main text). C–F, Absence of length differences in the innervation from the contralateral ear along the dorsoventral dimension of MSO. C, Hypothetical scheme of innervation by contralateral fibers, suggesting extra length for the most dorsally projecting (low-CF) fibers. If input fibers approach the MSO from ventral, low-CF fibers may have longer axonal length (arrow) to innervate the dorsal part of MSO than high-CF fibers for the ventral part. D, relationship between axonal length from ML to endpoints, and CF. Symbols in A and D indicate average axonal length; lines are range (A) and SD (D) for each projection (symbol color and shape as in Fig. 8). E, F, Coronal view of contralateral projections of fibers with lowest and highest CF (840 and 10,508 Hz, respectively).

ipsilateral reconstructions (i.e., where the length gradient was in the same direction as that of contralateral projections). This pattern was particularly convincing in the fiber with the lowest CF (200 Hz). Also, the rostrally directed delay line in the remaining four ipsilateral reconstructions was at least as steep (though of opposite sign) as that of the contralateral fibers (Figs. 8B, 14C), while in Beckius et al. (1999) the gradients on the ipsilateral side were shallow and constrained in rostrocaudal extent.

Anatomical patterns and best delays

Ultimately, "delay" is a functional concept requiring functional measurements. Particularly appealing in the morphological observations is their apparent consistency with the relationship between binaural tuning and cell location observed by Yin and Chan (1990), both in sign and in size. In that study, small best delays were found rostrally and large delays caudally, consistent with a caudally directed delay line contralaterally and/or a rostrally directed delay line ipsilaterally. Moreover, the range of physiological delays is reasonably in accord with estimated length differences and conduction speeds: a range of ~400 µs could be covered by combining "monaural" contralateral and ipsilateral delays.

Nevertheless, our quantitative analysis brings out several problems. Most importantly, there is nothing in the pattern of estimated delays observed that would suggest a CF-dependent range of delays (Fig. 14D). The anatomical branching patterns, as illustrated in Figures 2 and 3, are equally present at high and low CFs. In contrast, the physiological distribution of best delays measured in the MSO and inferior colliculus shows a clear depen-

dence on CF, in cat and in other mammals studied (Brand et al., 2002; McAlpine and Grothe, 2003; Hancock and Delgutte, 2004; Joris et al., 2006; Pecka et al., 2008).

A second problem, of relevance beyond the issue of axonal delay lines, is that of correct concatenation. None of the afferents illustrated here or in Beckius et al. (1999) innervates the entire rostrocaudal extent of the MSO. Thus, each tonotopic strip of MSO neurons must be supplied by a patchwork of afferents. This complicates the structural basis for a systematic rostrocaudal gradient, since it requires correct temporal stacking of collaterals. For example, contralateral projections 2 and 3 have the same CF but innervate different portions of the MSO: projection 2 is to the rostral half and shows a positive slope, while projection 3 is restricted toward the caudal pole (Figs. 8C, 14A). Obviously, if these two fibers were representative for a single animal, the delay pattern generated by projection 2 would not be complemented by the inputs from projection 3. In other cases, fibers of similar CF appear to concatenate in an orderly manner (e.g., contralateral projections 5, 6, and 7). The fibers labeled here were derived from different animals, and offsets in the ordinate values of Figures 8, C and D, and 14, A and B, could reflect differences in anatomy between animals (e.g., in MSO size and location). Within-animal data are reasonably consistent in one animal studied by Beckius et al. (1999, their Fig. 11) but not in the other, which showed large offsets among fibers. However, the latter case also showed large variation in dorsoventral location of the projections, so that the labeled population must reflect a wide range of CFs. Together, the available material does not allow a prediction of the degree of

temporal dispersion that may be present across afferents of equal CF.

A third problem may be in the range of delays. The estimated contralateral delays are small relative to the values of best delay observed, particularly at low CFs where best delays can be >1 ms (Fig. 14, upper hyperbole) (Hancock and Delgutte, 2004; Joris et al., 2006). Ipsilateral delays tend to be larger than contralateral delays but are also more erratic in sign and rostrocaudal coverage. Combination of contralateral and ipsilateral delays can enlarge the net interaural delay (when the slopes are of opposite sign for the contralateral and ipsilateral projections), but sources of delay in addition to the delays provided by the within-fiber branching pattern are needed to account for the full range of best delays observed at low CFs. We caution that the diameter measured on our material is necessarily a rough estimate, as is the relationship between fiber diameter and conduction speed (Waxman and Bennett, 1972), and is suited for observing trends rather than absolute values.

Our reanalysis casts doubts on the relevance of the rostrocaudal axonal branching patterns for interaural delay, but does not by itself contradict the evidence for a spatial map of delay in MSO (Yin and Chan, 1990). Nevertheless, taking into account the noise in the relationship observed by Yin and Chan (1990), the absence of a clear relationship in multiunit recordings (Oliver et al., 2003), and the problems in tying the distribution of best delays to axonal branching patterns (Fig. 14D), it appears increasingly doubtful that these patterns are an essential component of the binaural circuit.

A final qualification is that other features of the branching pattern—different from the simple within-axon delay line configuration—may contribute to internal delay. For example, contralateral/ipsilateral asymmetries in temporal dispersion, in convergence across CFs, and in convergence ratio could all contribute to the pattern of best delays observed. Also, based on our material we cannot exclude that patches of contralateral and ipsilateral fibers would provide the range of best delays observed (for comparison, see Goldberg and Brown, 1969). It is interesting in this regard that there is more consistency in the pattern of projections to the rostral than to the caudal half of MSO (Fig. 8). Finally, there are other determinants of conduction speed, internodal distance in particular, which may show systematic variations in mammalian binaural circuits, as in birds (Carr and Konishi, 1990; Seidl et al., 2010).

Tonotopy: over- or under-representation of low frequencies?
A surprising finding is the tonotopic distribution of afferents. Their layering suggests that low frequencies are under-represented rather than over-represented in the MSO. This is puzzling—functionally and anatomically—and is inconsistent with the "duplex" organization of the superior olivary complex (Irvine, 1986), comprising a low-frequency circuit computing ITD and a high-frequency circuit computing interaural level differences (ILDs). Taking the limited sample sizes of our data and those of Guinan et al. (1972) into account, a conservative statement is that MSO is tonotopically mapped isomorphic to the cochlea and has a low-frequency bias to the extent that very high CFs are not represented in MSO. The main duplex asymmetry is in the ILD (not the ITD) circuit: the lateral superior olive and medial nucleus of the trapezoid body show an apparent over-representation of high frequencies (Guinan et al., 1972).

References

Adams JC (1981) Heavy metal intensification of DAB-based HRP reaction product. J Histochem Cytochem 29:775.

Beckius GE, Batra R, Oliver DL (1999) Axons from anteroventral cochlear nucleus that terminate in medial superior olive of cat: observations related to delay lines. J Neurosci 19:3146–3161.

Bonham BH, Lewis ER (1999) Localization by interaural time difference (ITD): effects of interaural frequency mismatch. J Acoust Soc Am 106:281–290.

Brand A, Behrend O, Marquardt T, McAlpine D, Grothe B (2002) Precise inhibition is essential for microsecond interaural time difference coding. Nature 417:543–547.

Brownell WE (1975) Organization of the cat trapezoid body and the discharge characteristics of its fibers. Brain Res 94:413–433.

Cariani PA (2004) Temporal codes and computations for sensory representation and scene analysis. IEEE Trans Neural Netw 15:1100–1111.

Carr CE, Konishi M (1988) Axonal delay lines for time measurement in the owl's brainstem. Proc Natl Acad Sci U S A 85:8311–8315.

Carr CE, Konishi M (1990) A circuit for detection of interaural time differences in the brain stem of the barn owl. J Neurosci 10:3227–3246.

Goldberg JM, Brown PB (1969) Response of binaural neurons of dog superior olivary complex to dichotic tonal stimuli: some physiological mechanisms of sound localization. J Neurophysiol 22:613–636.

Greenwood DD (1990) A cochlear frequency-position function for several species 29 years later. J Acoust Soc Am 87:2592–2605.

Grothe B (2003) New roles for synaptic inhibition in sound localization. Nat Rev Neurosci 4:540–550.

Guinan JJ, Norris BE, Guinan SS (1972) Single auditory units in the superior olivary complex. II: locations of unit categories and tonotopic organization. Int J Neurosci 4:147–166.

Hancock KE, Delgutte B (2004) A physiologically based model of interaural time difference discrimination. J Neurosci 24:7110–7117.

Irvine DRF (1986) The auditory brainstem: a review of the structure and function of auditory brainstem processing mechanisms. Berlin: Springer.

Jeffress LA (1948) A place theory of sound localization. J Comp Physiol Psychol 41:35–39.

Joris P, Yin TC (2007) A matter of time: internal delays in binaural processing. Trends Neurosci 30:70–78.

Joris PX (1996) Envelope coding in the lateral superior olive. II. Characteristic delays and comparison with responses in the medial superior olive. J Neurophysiol 76:2137–2156.

Joris PX (2006) A dogged pursuit of coincidence. J Neurophysiol 96:969–972.

Joris PX, Yin TC (1998) Envelope coding in the lateral superior olive. III. Comparison with afferent pathways. J Neurophysiol 79:253–269.

Joris PX, Smith PH, Yin TC (1998) Coincidence detection in the auditory system: 50 years after Jeffress. Neuron 21:1235–1238.

Joris PX, Van de Sande B, Louage DH, van der Heijden M (2006) Binaural and cochlear disparities. Proc Natl Acad Sci U S A 103:12917–12922.

Liberman MC (1982) The cochlear frequency map for the cat: labeling auditory-nerve fibers of known characteristic frequency. J Acoust Soc Am 72:1441–1449.

Licklider JCR (1959) Three auditory theories. In: Psychology: a study of a science (Koch S, ed), pp 41–144. New York: McGraw-Hill.

McAlpine D (2005) Creating a sense of auditory space. J Physiol 566:21–28.

McAlpine D, Grothe B (2003) Sound localization and delay lines—do mammals fit the model? Trends Neurosci 26:347–350.

McAlpine D, Jiang D, Palmer AR (1996) Interaural delay sensitivity and the classification of low best-frequency binaural responses in the inferior colliculus of the guinea pig. Hear Res 97:136–152.

McAlpine D, Jiang D, Palmer AR (2001) A neural code for low-frequency sound localization in mammals. Nat Neurosci 4:396–401.

McFadden D (1973) Precedence effects and auditory cells with long characteristic delays. J Acoust Soc Am 54:528–530.

Oliver DL, Beckius GE, Bishop DC, Loftus WC, Batra R (2003) Topography of interaural temporal disparity coding in projections of medial superior olive to inferior colliculus. J Neurosci 23:7438–7449.

Palmer AR (2004) Reassessing mechanisms of low-frequency sound localisation. Curr Opin Neurobiol 14:457–460.

Palmer A, Kuwada S (2005) Binaural and spatial coding in the inferior colliculus. In: The inferior colliculus (Winer JA, Schreiner CE, eds), pp 377–410. New York: Springer.

Pecka M, Brand A, Behrend O, Grothe B (2008) Interaural time difference processing in the mammalian medial superior olive: the role of glycinergic inhibition. J Neurosci 28:6914–6925.

Rose JE, Gross NB, Geisler CD, Hind JE (1966) Some neural mechanisms in the inferior colliculus of the cat which may be relevant to localization of a sound source. J Neurophysiol 29:288–314.

Roth GL, Kochhar RK, Hind JE (1980) Interaural time differences: implications regarding the neurophysiology of sound localization. J Acoust Soc Am 68:1643–1651.

Schroeder MR (1977) New viewpoints in binaural interactions. In: Psychophysics and physiology of hearing (Evans EF, Wilson JP, eds), pp 455–467. New York: Academic.

Seidl AH, Rubel EW, Harris DM (2010) Mechanisms for adjusting interaural time differences to achieve binaural coincidence detection. J Neurosci 30:70–80.

Shamma SA, Shen NM, Gopalaswamy P (1989) Stereausis: binaural processing without neural delays. J Acoust Soc Am 86:989–1006.

Smith PH, Joris PX, Carney LH, Yin TC (1991) Projections of physiologically characterized globular bushy cell axons from the cochlear nucleus of the cat. J Comp Neurol 304:387–407.

Smith PH, Joris PX, Yin TC (1993) Projections of physiologically characterized spherical bushy cell axons from the cochlear nucleus of the cat: evidence for delay lines to the medial superior olive. J Comp Neurol 331:245–260.

Stotler WA (1953) An experimental study of the cells and connections of the superior olivary complex of the cat. J Comp Neurol 98:401–431.

Tollin DJ, Yin TC (2005) Interaural phase and level difference sensitivity in low-frequency neurons in the lateral superior olive. J Neurosci 25: 10648–10657.

Wagner H, Asadollahi A, Bremen P, Endler F, Vonderschen K, von Campenhausen M (2007) Distribution of interaural time difference in the barn owl's inferior colliculus in the low- and high-frequency ranges. J Neurosci 27:4191–4200.

Waxman SG, Bennett MV (1972) Relative conduction velocities of small myelinated and nonmyelinated fibers in the central nervous system. Nat New Biol 238:217–219.

Yin TC, Chan JC (1990) Interaural time sensitivity in medial superior olive of cat. J Neurophysiol 64:465–488.

Original Paper

ORL

Evaluation of the Carhart Effect in Congenital Middle Ear Malformation with Both an Intact External Ear Canal and a Mobile Stapes Footplate

Takashi Sakamoto[a]   Akinobu Kakigi[a]   Akinori Kashio[a]   Kaori Kanaya[a]
Mitsuya Suzuki[b]   Tatsuya Yamasoba[a]

[a]Department of Otolaryngology and Head and Neck Surgery, Graduate School of Medicine, Faculty of Medicine, University of Tokyo, Tokyo, and [b]Department of Otolaryngology and Head and Neck Surgery, Sakura Medical Center, University of Toho, Chiba, Japan

Abstract
The medical charts of 41 ears with congenital middle ear malformation with both an intact external ear canal and a mobile stapes footplate were reviewed retrospectively to study the Carhart effect. The operations were categorized as successful or unsuccessful according to the extent of decrease in the average air-bone gap. Statistically significant differences were observed between the 2 groups with respect to the changes in pure-tone average and the changes in the bone conduction (BC) threshold at 1 and 2 kHz. Linear regression analysis revealed weak correlations between the change in the BC threshold and the postoperative BC threshold at an overall level and at the 4 frequencies tested. Stapes ankylosis is a main cause of the Carhart effect. The present study showed that in congenital middle ear malformation, the Carhart effect was caused not only by stapes ankylosis but also by other types of disruption in the ossicular chain.

Copyright © 2011 S. Karger AG, Basel

Introduction

A middle ear abnormality causes a gap between the air and bone conduction (BC) thresholds and is often accompanied by a depression of the BC thresholds. This phenomenon was first reported by Carhart [1] in 1949. Later, he demonstrated an improvement in the BC threshold after successful fenestration surgery for otosclerosis, and this depression in the BC threshold was designated the Carhart notch. In the report, the depression was maximal at 2 kHz and ranged in frequency from 0.5 to 4 kHz. Therefore, it is suitable to designate the phenomenon Carhart effect instead of the Carhart notch [2].

The Carhart effect was also described in malleus fixation, otitis media with effusion, chronic otitis media, cholesteatoma, and congenital malformation of the middle ear [3–8]. The mechanism responsible for the Carhart effect is still not clearly understood, but it is attributed to a decrease in the external and middle ear components of BC transmission. In patients with a middle ear abnormality, it is difficult to distinguish whether the elevation of the BC threshold is true or false before surgery. If the BC thresholds are misunderstood, a surgeon may misjudge an indication for surgical intervention. Therefore, it is important to assess the Carhart effect in detail.

Takashi Sakamoto
Department of Otolaryngology and Head and Neck Surgery
Graduate School of Medicine, Faculty of Medicine, The University of Tokyo
Hongo 7-3-1, Bunkyo-ku, Tokyo 113-8655 (Japan)
Tel. +81 3 5800 8924, Fax +81 3 3814 9486, E-Mail tsakamoto-tky@umin.ac.jp

Congenital malformation of the middle ear is accompanied by various types of abnormalities in the middle ear, such as ossicular ankylosis, which includes a fixed stapes footplate, and disruption in the ossicular joint [9], but it is rarely accompanied by inflammatory lesions such as tympanosclerosis and the formation of granulation tissue. Therefore, congenital malformation of the middle ear with a mobile stapes footplate is an appropriate pathological lesion for evaluating the Carhart effect. It is well known that ankylosis of the stapes footplate causes the Carhart effect. However, to our knowledge, few reports have evaluated the Carhart effect in a series of patients with congenital malformation of the middle ear with a mobile stapes footplate. The present study aimed to evaluate differences in the change in BC thresholds at 0.5, 1, 2, and 4 kHz between successful and unsuccessful surgery groups. We also evaluated the correlations between the changes in the BC thresholds and the postoperative BC thresholds at an overall level and at the 4 frequencies by using linear regression analysis.

Materials and Methods

In this study, we examined 36 patients with congenital middle ear malformation with both an intact external ear canal and a mobile stapes footplate; 5 of these patients were affected bilaterally and 31 were affected unilaterally. Forty-one ears were operated by tympanoplasty at the Hospital of the University of Tokyo, and medical charts were retrospectively reviewed. This study was approved by the Ethics Committee of the University of Tokyo. All patients underwent a complete clinical examination, which included pure-tone audiometry, tympanometry with stapedial reflex, and a high-resolution temporal bone computed tomography. The diagnosis was confirmed in all cases during surgery. All patients included in the study had at least 1 year of follow-up.

Tympanoplasty was performed via the transcanal or retroauricular approach under general anesthesia. In tympanoplasty, the ossicular chain was reconstructed with autografts including the incus removed or tragal cartilage.

Pure-tone audiometry was conducted periodically (1 month after the operation and then every 2 months, for a minimum of 1 year after surgery). The preoperative and postoperative pure-tone average (PTA) values were calculated as the mean air conduction (AC) threshold at 0.5, 1, 2, and 4 kHz. The change in PTA was calculated as preoperative minus postoperative PTA. Cases whose average air-bone gap at 0.5, 1, 2, and 4 kHz decreased to within 20 dB were regarded as having a successful surgery, according to the guidelines of the Committee on Hearing and Equilibrium [10]. The ears operated were classified into successful and unsuccessful surgery groups. Congenital ossicular anomalies were divided into 5 categories according to the classification of Park and Choung [9]. In brief, type 1 includes patients with a normal stapes and an anomaly of the incus or malleus. Type 2 includes patients with a mobile footplate and other anomalies. Type 3 includes patients

Table 1. Demographic data of the successful and unsuccessful surgery groups

	Successful surgery group	Unsuccessful surgery group
Number of ears	23	18
Mean age at operation ± SD years	28.5 ± 20.1	17.6 ± 10.8
Sex (male/female)	12/11	9/9
Side of operation (right/left)	7/16	7/11
Type 1 malformation (ears)	20	14
Type 2 malformation (ears)	3	4

The 2 groups did not differ in terms of age at operation, sex, side of the operation, and the distribution of types of ossicular malformation.

with stapes footplate fixation only. Type 4 includes patients with stapes footplate fixation and other anomalies. Type 5 includes patients with no stapes footplate and other anomalies. Types 1 and 2 were considered to have a mobile stapes footplate. Types 3, 4, and 5 were considered to have a fixed stapes footplate. Patients with types 1 and 2 disease were enrolled in the present study.

The change in the BC threshold was calculated as preoperative minus postoperative BC threshold at 0.5, 1, 2, and 4 kHz in pure-tone audiometry.

Differences in the preoperative PTA, the postoperative PTA, the change in the PTA and the BC threshold at 0.5, 1, 2, and 4 kHz between the successful and unsuccessful surgery groups were analyzed by using the Mann-Whitney test. Differences between the preoperative and postoperative BC thresholds at 0.5, 1, 2, and 4 kHz in each group were analyzed by using the Wilcoxon test. A p value of <0.05 was considered statistically significant.

We also evaluated the correlations between the change in the BC threshold and the postoperative BC threshold at an overall level and at the 4 tested frequencies by using linear regression analysis. Pearson's correlation coefficients between the 2 parameters were calculated.

Results

Table 1 presents the demographic data of the patients. In the successful surgery group, patients were aged 27.8 ± 20.0 years (mean ± SD). In the unsuccessful surgery group, patients were aged 21.8 ± 14.0 years (mean ± SD). The successful and unsuccessful surgery groups included 31 and 18 ears, respectively. Of the 23 ears in the successful surgery group, 12 were of male patients and 11 were of female patients, and 7 were right ears and 16 were left ears. Of the 18 ears in the unsuccessful surgery group, 9 were of male patients and 9 were of female patients, and 7 were right ears and 11 were left ears.
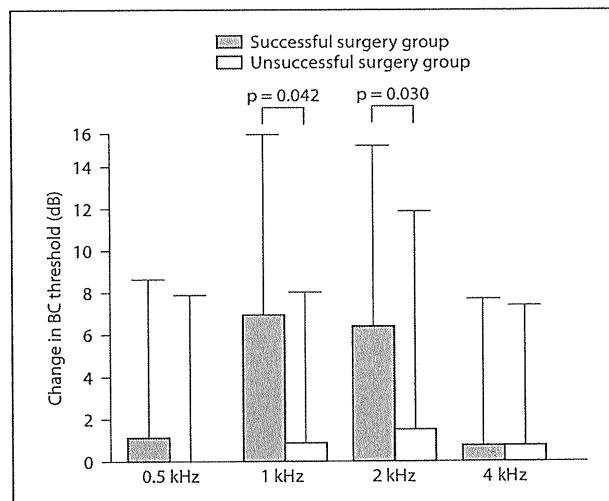
Sakamoto/Kakigi/Kashio/Kanaya/
Suzuki/Yamasoba
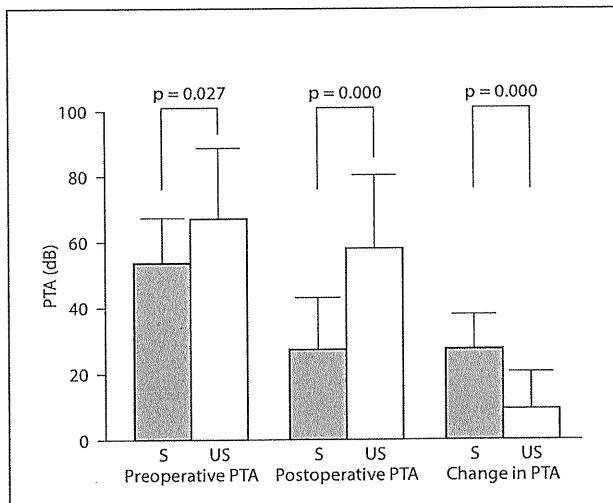
Fig. 1. The preoperative PTAs in the successful and unsuccessful surgery groups were 53.8 ± 14.5 and 66.9 ± 22.6 dB HL (mean ± SD), respectively. The p value revealed by the Mann-Whitney test for preoperative PTA was 0.027. The postoperative PTAs in the successful and unsuccessful surgery groups were 26.9 ± 16.0 and 57.8 ± 22.5 dB HL (mean ± SD), respectively. The p value revealed by the Mann-Whitney test for postoperative PTA was 0.000. The changes in PTA in the successful and unsuccessful surgery groups were 27.0 ± 10.6 and 9.1 ± 11.6 dB HL (mean ± SD), respectively. The p value revealed by the Mann-Whitney test for the difference in postoperative PTA was 0.000. Statistically significant differences in the preoperative and postoperative PTAs, and the changes in PTA between the successful and unsuccessful surgery groups were detected. S = Successful surgery group; US = unsuccessful surgery group.

Fig. 2. In the successful surgery group, the changes in BC threshold at 0.5, 1, 2, and 4 kHz were 1.1 ± 7.6, 7.1 ± 8.8, 6.5 ± 8.9, and 1.1 ± 7.2 dB HL (mean ± SD), respectively. In the unsuccessful surgery group, the changes in BC threshold at 0.5, 1, 2, and 4 kHz were 0.0 ± 8.0, 0.83 ± 7.3, 1.5 ± 10.6, and 1.1 ± 6.8 dB HL (mean ± SD), respectively. The p values revealed by the Mann-Whitney test for the change in BC thresholds at 0.5, 1, 2, and 4 kHz were 0.378, 0.042, 0.030, and 0.915, respectively. Statistically significant differences for the change in BC threshold between the successful and unsuccessful surgery groups were identified at 1 and 2 kHz.

In the successful surgery group, type 1 and 2 anomalies included 20 and 3 ears, respectively. In the unsuccessful surgery group, type 1 and 2 anomalies included 14 and 4 ears, respectively.

The preoperative PTAs in the successful and unsuccessful surgery groups were 53.8 ± 14.5 and 66.9 ± 22.6 dB HL (mean ± SD), respectively. The p value for the Mann-Whitney test for preoperative PTA was 0.027 (fig. 1). Statistically significant differences in preoperative PTA between the successful and unsuccessful surgery groups were found.

The postoperative PTAs in the successful and unsuccessful surgery groups were 26.9 ± 16.0 and 57.8 ± 22.5 dB HL (mean ± SD), respectively. The p value revealed by the Mann-Whitney test for the difference in postoperative PTA was 0.000 (fig. 1). A statistically significant difference in postoperative PTA between the successful and unsuccessful surgery groups was found.
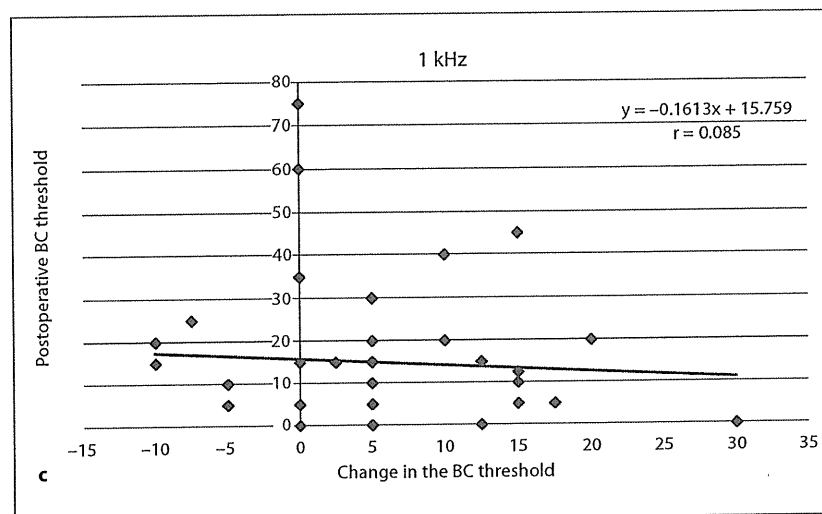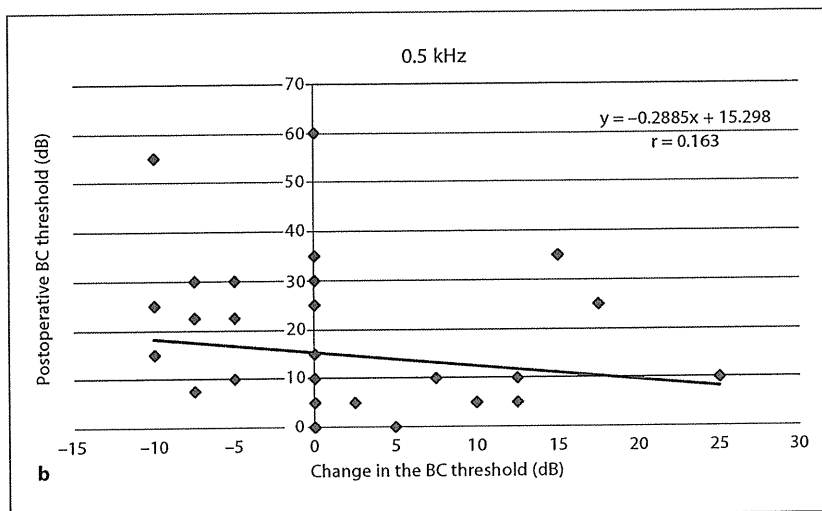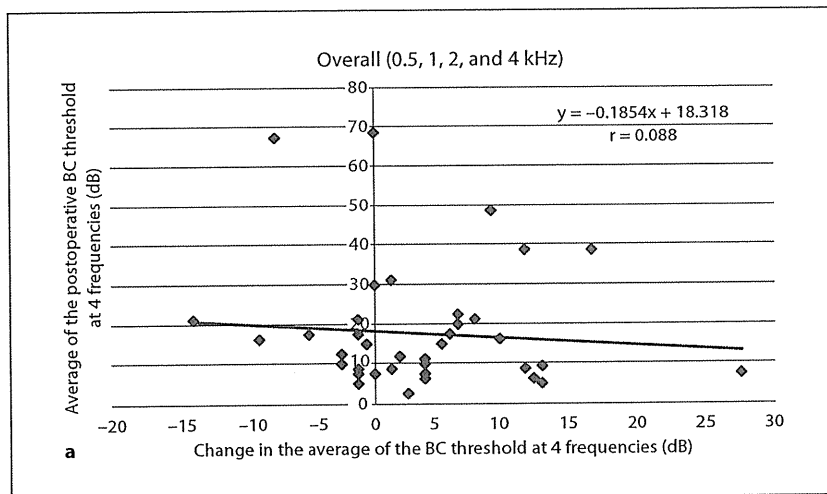
The changes of PTA in the successful and unsuccessful surgery groups were 27.0 ± 10.6 and 9.1 ± 11.6 dB HL (mean ± SD), respectively. The p value revealed by the Mann-Whitney test for the difference in postoperative PTA was 0.000 (fig. 1). The changes in PTA differed significantly between the successful and unsuccessful surgery groups.

In the successful surgery group, the preoperative BC thresholds at 0.5, 1, 2, and 4 kHz were 13.5 ± 11.7, 16.5 ± 15.1, 23.8 ± 17.6, and 18.0 ± 15.5 dB HL (mean ± SD), respectively. The postoperative BC thresholds at 0.5, 1, 2, and 4 kHz were 12.6 ± 11.9, 9.5 ± 12.8, 17.3 ± 17.1, and 17.0 ± 14.5 dB HL (mean ± SD), respectively. The p values revealed by the Wilcoxon test for differences between preoperative and postoperative BC thresholds at 0.5, 1, 2, and 4 kHz were 0.507, 0.002, 0.004, and 0.453, respectively. Statistically significant differences were found at 1 and 2 kHz.

In the unsuccessful surgery group, the preoperative BC thresholds at 0.5, 1, 2, and 4 kHz were 18.6 ± 17.4, 23.1 ± 20.7, 30.4 ± 20.2, and 26.3 ± 20.0 dB HL (mean ± SD), respectively. The postoperative BC thresholds at

Overall (0.5, 1, 2, and 4 kHz)

$y = -0.1854x + 18.318$
$r = 0.088$

Average of the postoperative BC threshold at 4 frequencies (dB)

Change in the average of the BC threshold at 4 frequencies (dB)

a

0.5 kHz

$y = -0.2885x + 15.298$
$r = 0.163$

Postoperative BC threshold (dB)

Change in the BC threshold (dB)

b

1 kHz

$y = -0.1613x + 15.759$
$r = 0.085$

Postoperative BC threshold

Change in the BC threshold

c

Fig. 3. a Linear regression analysis revealed weak correlations between the changes in the average BC threshold at 0.5, 1, 2, and 4 kHz and the average postoperative BC thresholds at the 4 frequencies. Pearson's correlation coefficient was 0.088. b–e Linear regression analysis revealed a weak correlation between the change in the BC threshold and the postoperative BC threshold at the 4 frequencies (b: 0.5 kHz, c: 1 kHz, d: 2 kHz, e: 4 kHz). Pearson's correlation coefficients at 0.5, 1, 2, and 4 kHz were 0.163, 0.085, 0.167, and 0.157, respectively.

0.5, 1, 2, and 4 kHz were 19.2 ± 15.0, 22.2 ± 18.0, 28.9 ± 17.2, and 23.8 ± 20.5 dB HL (mean ± SD), respectively. The p values revealed by the Wilcoxon test for differences between preoperative and postoperative BC thresholds at 0.5, 1, 2, and 4 kHz were 0.380, 0.750, 0.968, and 0.418, respectively. No statistically significant differences were found at any frequency.

In the successful surgery group, the changes in BC thresholds at 0.5, 1, 2, and 4 kHz were 1.1 ± 7.6, 7.1 ± 8.8, 6.5 ± 8.9, and 1.1 ± 7.2 dB HL (mean ± SD), respectively. In the unsuccessful surgery group, the changes in BC thresholds at 0.5, 1, 2, and 4 kHz were 0.0 ± 8.0, 0.83 ± 7.3, 1.5 ± 10.6, and 1.1 ± 6.8 dB HL (mean ± SD), respectively. The p values revealed by the Mann-Whitney

test for the change in BC thresholds at 0.5, 1, 2 and 4 kHz were 0.378, 0.042, 0.030, and 0.915, respectively. Statistically significant differences for the change in the BC threshold between the successful and unsuccessful surgery groups were found at 1 and 2 kHz (fig. 2).

In linear regression analysis, Pearson's correlation coefficients at the overall level and at 0.5, 1, 2, and 4 kHz were 0.088, 0.161, 0.085, 0.167, and 0.157, respectively. The corresponding adjusted coefficients of determination (R^2) were −0.018 and 0.001, −0.018, 0.003, and 0.000. Linear regression analysis revealed positive but weak correlations between the changes in the BC threshold and the postoperative BC threshold at the overall level and at the 4 frequencies (fig. 3a–e).
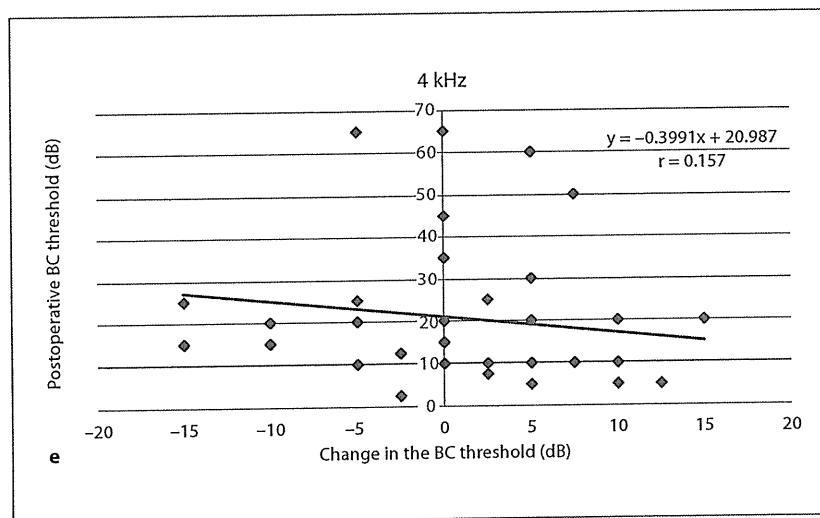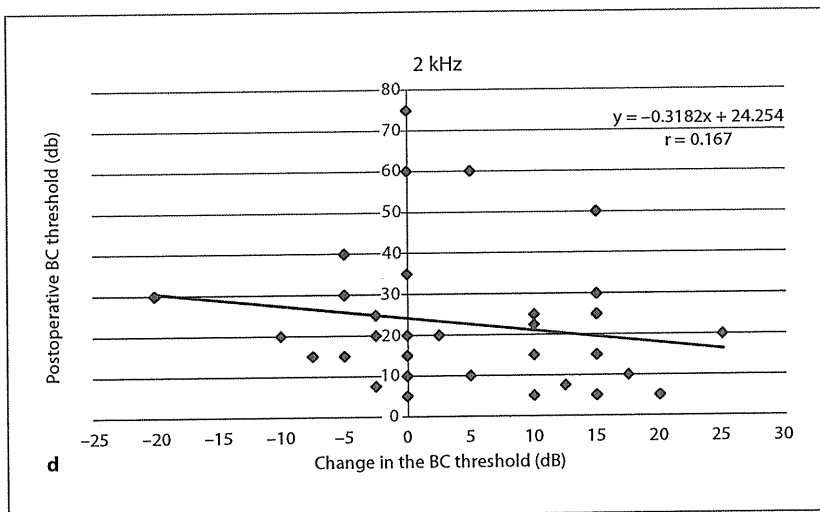
Discussion

In the present study, the Carhart effect in the successful surgery group was greater than that in the unsuccessful surgery group at 0.5, 1, and 2 kHz. However, statistically significant differences in the Carhart effect between the successful and unsuccessful surgery groups were identified at 1 and 2 kHz, and the Carhart effect at 1 kHz was slightly greater than that at 2 kHz. This study is the first to evaluate the Carhart effect in a series of patients having isolated congenital ossicular anomalies with a mobile stapes footplate.

The BC response employs 3 different modes: the compressional, inertial, and osseotympanic modes [11]. In the compressional mode, skull vibration caused by sound directly causes vibration of the otic capsule. In the inertial mode, skull vibration caused by sound induces movement in the ossicular chain due to the inertial force of the ossicles. In the osseotympanic mode, sound energy causes vibration of the skull and para-auditory structures (i.e. jaw and soft tissue), and these vibrations are transmitted from the external auditory canal to the ossicles through the tympanic membrane [12]. The disruption of the ossicular chain may prevent the effect of the inertial and osseotympanic modes, and this is thought to be the main cause of the Carhart effect.

In Carhart's classic report, the maximal elevation of the BC threshold was observed at 2 kHz and the elevation of BC was described in the range of frequencies from 0.5 to 4 kHz [2]. The range of frequencies in which the Carhart effect exists is controversial. Variations in the Carhart notch ranging from 0.5 to 4 kHz were reported in patients with otosclerosis [13]. Ginsberg et al. [14] reported that the effect in a large series of patients who underwent stapedectomy was approximately equal in frequencies between 0.5 and 2 kHz (15–18 dB). Cook et al. [15] reported that in 102 patients who underwent stapedectomy, linear regression analysis revealed significant linear relationships between the gain in the AC threshold and the gain in the BC threshold at 0.5, 1, 2, and 4 kHz, concluding that the Carhart effect was most prominent at 2 kHz, because the gradient of the regression line was steepest at 2 kHz.

The Carhart effect has also been described in malleus fixation, otitis media with effusion, chronic otitis media, and congenital malformation of the middle ear [3–8]. In contrast to otosclerosis, there are few reports that assess the Carhart effect in a large series of patients with congenital ossicular anomalies. Isolated congenital ossicular anomalies can affect the ossicular chain in a wide range of modes, including ossicular ankylosis and disruption in

the ossicular joint [9]. Therefore, reconstruction surgery for this condition is not as simple as that when done for otosclerosis and may involve a variety of operations from tympanoplasty to the release of ossicular ankylosis.

Yasan [16] assessed the change in the BC threshold after tympanoplasty for otosclerosis, tympanosclerosis, chronic otitis media, and a few cases of congenital ossicular anomalies and reported that the Carhart notch at 2 kHz indicated stapes footplate fixation, but that the Carhart notch at 1 kHz indicated a mobile stapes footplate. Their results disagree with our results because in the present study, the Carhart effect was observed at both 1 and 2 kHz in anomalies with a mobile footplate. Lee et al. [6] reported that the BC thresholds at 0.5, 1, 2, and 4 kHz were significantly improved after tympanoplasty for chronic otitis media, and the greatest improvement was observed at 2 kHz. In contrast, in the present study, a significant improvement in the BC threshold was identified at both 1 and 2 kHz, and the improvement at 1 kHz was slightly greater than that at 2 kHz. Moreover, the Carhart effect was not observed at 0.5 and 4 kHz. These results are inconsistent with the results of Lee et al. One possible explanation for the discrepancy between their results and ours is a difference in inclusion criteria. In the inclusion criteria of Lee et al., successful surgery was defined as an improvement in the mean of the AC threshold of 15 dB or more. In our inclusion criteria, however, successful surgery was defined as a decrease in the average air-bone gap at 0.5, 1, 2, and 4 kHz to within 20 dB according to the guidelines of the Committee on Hearing and Equilibrium [10]. The criteria of Lee et al. ensure that a real improvement has occurred after surgery, while our criteria generally ensure that the middle ear component is as near normal as possible. In our study, the change in PTA in the successful surgery group was significantly greater than that in the unsuccessful surgery group. This result demonstrates that our criteria properly reflect a real improvement in hearing and suggest that our criteria may be more stringent than the criteria of Lee et al.

Inclusion criteria are necessary for this kind of analysis. Unless appropriate inclusion criteria are applied, an analysis may lead to an underestimation of the Carhart effect [17].

In the present study, a significant improvement in the BC threshold was not identified at 4 kHz. The reason remains unsolved, but the deterioration of the BC threshold due to inner ear damage by surgery may be involved.

One possible explanation for the nonsignificance of the improvement in the BC threshold at 0.5 kHz is the occlusion effect of the external ear canal. In the open ear

Sakamoto/Kakigi/Kashio/Kanaya/
Suzuki/Yamasoba

canal, the sound pressure generated by BC is smaller than the threshold level. Sound pressure in the external ear canal caused by BC stimuli is elevated below 1 kHz when the external ear canal is occluded; this is called the occlusion effect [18–21] and is estimated to be up to 20 dB [22]. There remains the possibility that our result at 0.5 kHz was influenced by an underestimation of the Carhart effect because of the occlusion effect.

Moreover, surgical interventions cannot completely restore normal transmission of sound energy from the tympanic membrane to the oval window, and thus, postoperative BC thresholds may still include a residual Carhart effect. Hence, any method using preoperative and postoperative BC threshold is liable to underestimate the magnitude of the Carhart effect.

In the present study, linear regression analysis revealed positive but weak correlations between the changes in the BC threshold and the postoperative BC threshold at the overall level and at the 4 frequencies, although the significant Carhart notch was noted only at 1 and 2 kHz in the Mann-Whitney test. This discrepancy may be attributed to the difference in the methodology of statistical analysis. A relatively small sample size does not affect the statistical power of the nonparametric Mann-Whitney test. In contrast, to retain the statistical power, a larger sample size is required for linear regression analysis than for the Mann-Whitney test. Sample size in the present study was unlikely to be large enough for linear regression analysis to show a large correlation coefficient.

It is important to note that one should understand the true BC thresholds before ear surgery for congenital middle ear malformation with both an intact external ear canal and a mobile stapes footplate. Otherwise patients may miss an opportunity to have their hearing restored because surgeons may dismiss the idea of surgery due to a poor functional result.

In summary, the present study found that the Carhart effect was statistically significant at 1 and 2 kHz, and that the Carhart effect was slightly greater at 1 kHz than at 2 kHz. However, the occlusion effect may have caused the Carhart effect at 0.5 kHz to be underestimated. These results suggest that the deterioration of the BC threshold in congenital middle ear malformation with an intact external ear canal is caused not only by stapes ankylosis, but also by other kinds of disruption in the ossicular chain, and that the Carhart effect was identified at at least 2 frequencies even in the absence of a fixed stapes footplate.

Acknowledgement

References

1 Carhart R, Hayes C: Clinical reliability of bone conduction audiometry. Laryngoscope 1949;59:1084–1101.
2 Carhart R: Clinical application of bone conduction audiometry. Arch Otolaryngol 1950; 51:798–808.
3 Ahmad I, Pahor AL: Carhart's notch: a finding in otitis media with effusion. Int J Pediatr Otorhinolaryngol 2002;64:165–170.
4 Austin DF: Sound conduction of the diseased ear. J Laryngol Otol 1978;92:367–393.
5 Conijn EA, Van der Drift JF, Brocaar MP, Van Zanten GA: Conductive hearing loss assessment in children with otitis media with effusion. A comparison of pure tone and bera results. Clin Otolaryngol Allied Sci 1989;14: 115–120.
6 Lee HS, Hong SD, Hong SH, Cho YS, Chung WH: Ossicular chain reconstruction improves bone conduction threshold in chronic otitis media. J Laryngol Otol 2008;122: 351–356.
7 Moon CN Jr, Hahn MJ: Primary malleus fixation: diagnosis and treatment. Laryngoscope 1981;91:1298–1307.

8 Tuz M, Dogru H, Uygur K, Gedikli O: Improvement in bone conduction threshold after tympanoplasty. Otolaryngol Head Neck Surg 2000;123:775–778.
9 Park K, Choung YH: Isolated congenital ossicular anomalies. Acta Otolaryngol 2009; 129:419–422.
10 Committee on hearing and equilibrium guidelines for the evaluation of results of treatment of conductive hearing loss. American Academy of Otolaryngology-Head and Neck Surgery Foundation, Inc. Otolaryngol Head Neck Surg 1995;113:186–187.
11 Tonndorf J: A new concept of bone conduction. Arch Otolaryngol 1968;87:595–600.
12 Tsai V, Ostroff J, Korman M, Chen JM: Bone-conduction hearing and the occlusion effect in otosclerosis and normal controls. Otol Neurotol 2005;26:1138–1142.
13 Perez R, de Almeida J, Nedzelski JM, Chen JM: Variations in the 'Carhart notch' and overclosure after laser-assisted stapedotomy in otosclerosis. Otol Neurotol 2009;30:1033–1036.
14 Ginsberg IA, Hoffman SR, Stinziano GD, White TP: Stapedectomy – In-depth analysis of 2,405 cases. Laryngoscope 1978;88:1999–2016.

15 Cook JA, Krishnan S, Fagan PA: Quantifying the Carhart effect in otosclerosis. Clin Otolaryngol Allied Sci 1995;20:258–261.
16 Yasan H: Predictive role of Carhart's notch in pre-operative assessment for middle-ear surgery. J Laryngol Otol 2007;121:219–221.
17 Gatehouse S, Browning GG: A re-examination of the Carhart effect. Br J Audiol 1982; 16:215–220.
18 Huizing EH: Bone conduction-the influence of the middle ear. Acta Otolaryngol Suppl 1960;155:1–99.
19 Khanna SM, Tonndorf J, Queller JE: Mechanical parameters of hearing by bone conduction. J Acoust Soc Am 1976;60:139–154.
20 Stenfelt S, Wild T, Hato N, Goode RL: Factors contributing to bone conduction: the outer ear. J Acoust Soc Am 2003;113:902–913.
21 Tonndorf J: Bone conduction. Studies in experimental animals. Acta Otolaryngol 1966;Suppl 213:1+.
22 Stenfelt S, Goode RL: Bone-conducted sound: physiological and clinical aspects. Otol Neurotol 2005;26:1245–1261.

Drug Delivery System

Offprint

Title

_____

_____

Name

_____

Department

Institution

Address

| Postal Code | City | Country |

| Phone | | Fax |

_____